Composite Structures 383 (2026) 120185

Contents lists available at ScienceDirect

Composite Structures

journal homepage: www.elsevier.com/locate/compstruct

A multiscale modeling framework for predicting the viscoelastic–plastic behavior of thin-walled composite deployable structures

Xiaowei Yue [a], Ruiwen Guo [b], Ning An [c,*], Hao Jin [d], Jinxiong Zhou [a,*]

[a] State Key Laboratory for Strength and Vibration of Mechanical Structures, School of Aerospace, Xi'an Jiaotong University, Xi'an 710049, People's Republic of China
[b] Xi'an Institute of Space Radio Technology, Xi'an 710100, People's Republic of China
[c] Robotic Satellite Key Laboratory of Sichuan Province, Key Laboratory of Advanced Spatial Mechanism and Intelligent Spacecraft, Ministry of Education, School of Aeronautics and Astronautics, Sichuan University, Chengdu 610065, People's Republic of China
[d] School of Mechanical Engineering, Hangzhou Dianzi University, Hangzhou 310018, People's Republic of China

ARTICLE INFO

Dataset link: https://github.com/XJTU-Zhou-group/ABAQUS_UMAT_HSCmultiscaleVEP

Keywords:
High-strain composites
Multiscale modeling
Viscoelastic–plastic
Deployable structures

ABSTRACT

Thin-walled composite deployable structures have garnered significant attention in space applications due to their unique folding and deployment capabilities. However, their long-term stowage and recovery performance is strongly influenced by viscoelastic–plastic (VE-P) behavior, which remains insufficiently understood due to the lack of rigorous modeling methodologies. To address this challenge, we develop a multiscale modeling framework to characterize the time-dependent and plastic responses of thin-ply high-strain composites employed in such structures. Constitutive VE-P models are formulated at multiple scales: an isotropic VE-P model is constructed for the polymer matrix, while two anisotropic VE-P models are developed for unidirectional fiber yarns and woven composite laminae. The polymer matrix parameters are calibrated using experimental data. Representative volume element (RVE) models at the microscale and mesoscale are employed to compute the effective VE-P properties of the unidirectional yarns and woven laminae, respectively. The anisotropic VE-P model is then implemented in finite element analyses to simulate the time-dependent and plastic behavior of the composite lamina, with predictions validated against experimental measurements. Finally, the constitutive model is applied at the macroscale to simulate the folding, stowage, deployment, and recovery processes of a particular thin-walled composite lenticular boom, capturing key behaviors such as shape recovery and permanent deformation. The results confirm the efficiency and reliability of the proposed multiscale approach for evaluating the stowage and recovery performance of composite deployable structures.

1. Introduction

Thin-walled composite deployable structures are increasingly employed in the construction of advanced large-scale space systems, such as solar arrays, deorbit sails, and starshades for astronomical observations [1–3]. These structures are typically fabricated from fiber-reinforced composite laminates composed of ultra-thin plies, commonly referred to as high-strain composites (HSCs) [4]. During operation, HSC-based deployable structures are bent from their nominal configurations into compact stowed states to minimize volume occupancy, and this stowed configuration is maintained until the spacecraft reaches its target orbit. The structures are then deployed back to their original shapes, driven either by the release of stored strain energy or by associated deployment mechanisms. The operation of such structures can generally be categorized into four distinct phases: folding, storage, deployment, and recovery. Experimental observations have revealed that HSC-based deployable structures exhibit pronounced time-dependent and plastic mechanical behaviors during the storage and recovery phases, which critically affects their long-term performance. Specifically, stress relaxation during extended storage can degrade the stored strain energy, thereby reducing deployment effectiveness and potentially leading to incomplete or failed deployment [5–8]. Furthermore, residual deformations are often observed after deployment—some of which are recoverable during the recovery period, while others remain as permanent deformations [7,9,10]. These residual deformations may compromise structural stiffness and load-carrying capacity and, in high-precision applications such as space antenna reflectors or spaceborne scientific instruments, even minor shape deviations can jeopardize mission success [1].

The time-dependent and plastic behavior exhibited by HSC-based deployable structures during their service life primarily originates from

* Corresponding authors.
E-mail addresses: anning@scu.edu.cn (N. An), jxzhouxx@mail.xjtu.edu.cn (J. Zhou).

https://doi.org/10.1016/j.compstruct.2026.120185
Received 5 November 2025; Received in revised form 21 January 2026; Accepted 22 February 2026
Available online 23 February 2026

the intrinsic viscoelasticity and plasticity of the polymer matrix within the composite materials [11–13]. The reinforcing fibers are typically considered purely elastic. Consequently, the overall mechanical response of the composite must be derived from the behavior of its constituents through suitable averaging techniques, often requiring a multiscale analysis framework. At the microscale, the effective properties of unidirectional fiber yarns are computed based on the interactions between the elastic fibers and the viscoelastic–plastic polymer matrix. At the mesoscale, the effective response of woven laminae is further derived from the properties of these yarns and the surrounding matrix. Finally, at the macroscale, the effective behavior of the woven lamina is employed to model the structural response of thin-walled composite shell structures. We note that such multiscale modeling approaches have been increasingly adopted in recent years for the analysis of deployable composite structures; however, most existing studies have been limited to capturing only their elastic and viscoelastic responses, while the incorporation of plasticity remains largely unexplored. For instance, Kueh and Pellegrino [14] developed a two-scale numerical homogenization strategy to determine the anisotropic linear elastic response of triaxially braided composites. This approach was later extended to plain-weave composites by Mallikarachchi [15], and further generalized to accommodate 2D weaves, 3D woven architectures, and multiaxial textiles through open-source computational tools developed by Jin et al. [16]. Kwok and colleagues [6,17] further advanced the two-step homogenization method to incorporate viscoelastic behavior by modeling the polymer matrix as a linearly viscoelastic material using the generalized Maxwell model. Similarly, Yu and colleagues introduced another numerical homogenization approach, termed the Mechanics of Structure Genome (MSG) method [18–20], to predict the macroscopic viscoelastic response of composite materials [21,22]. Overall, the multiscale method has been applied to study viscoelastic relaxation effects of a variety of thin-walled composite deployable structures. Examples includes tape-springs [23–25], bistable tape-spring hinges [26–28], lenticular booms [7], and reflector surfaces [29].

Despite these advancements, existing studies have not yet been fully extended to incorporate plasticity. Integrating plasticity into the analysis demands a rigorous framework capable of capturing not only the isotropic yielding and plastic behavior of the polymer matrix but also the anisotropic yielding and plastic responses of the unidirectional fiber yarns and woven composite laminae. Furthermore, accurately homogenizing the nonlinear, time-dependent, and plastic behavior across micro- and meso-scales to determine the effective anisotropic VE-P properties of the lamina remains a major challenge, owing to the inherent complexity of multiscale interactions and material heterogeneity. Early analytical studies proposed a variety of nonlinear anisotropic viscoelastic and viscoplastic constitutive models to accommodate the time-dependent and plastic behavior of fiber-reinforced composites. These include incremental formulations [30], tangent approaches [31], and affine schemes [32–35]. However, such analytical methods often rely on simplifying assumptions and are generally inadequate for capturing the complex microstructural features inherent to advanced composite systems. Alternatively, numerical simulations offer a more flexible and accurate approach, enabling the incorporation of realistic material architectures and facilitating closer collaboration between academic research and industrial applications. Among numerical methods, two primary categories can be identified. The first includes approaches that do not rely on predefined constitutive laws for the composite lamina. Notably, the FE^2 method and various data-driven techniques fall into this category. In FE^2, the macroscopic mechanical response at each integration point is computed directly from a representative volume element (RVE) that captures the underlying microstructural characteristics, thereby eliminating the need for explicit macroscopic constitutive assumptions [36–39]. In data-driven methods, the nonlinear stress–strain response is represented with trained artificial neural networks [40–45]. While offering high fidelity, these methods often entail significant computational costs, either by computation or generating database. The second category assumes that the composite lamina obeys a predefined continuum constitutive law. In this framework, RVE-based simulations are used to perform virtual mechanical tests that generate effective stress–strain data, which are then used to calibrate the constitutive parameters of the macroscopic model. This numerical homogenization approach offers a more computationally efficient alternative while still capturing essential microstructural effects. The resulting model retains the influence of microstructural features while avoiding the high computational burden associated with full FE^2 simulations. This numerical homogenization strategy has been widely adopted to model the nonlinear mechanical behavior of composites, particularly in the context of viscoelastic [13,46,47] and viscoplastic [48,49] responses.

To model the VE-P behavior of composites within a multiscale framework using numerical homogenization methods, several key challenges must be addressed. First, an isotropic VE-P constitutive model is required to accurately characterize the mechanical response of the polymer matrix. Second, two distinct anisotropic VE-P constitutive models must be developed to represent the behavior of unidirectional fiber yarns and woven laminae, respectively. Additionally, RVE analyses must be carefully designed and conducted to calibrate the effective anisotropic viscoelastic and plastic properties of the composite materials based on the known behavior of their constituent phases. Zhang et al. [50] carried out RVE analyses for unidirectional composites in which the fibers were modeled as linear elastic and the matrix as an isotropic viscoelastic–viscoplastic (VE-VP) material. While this approach successfully captured the VE-VP response of unidirectional composites, it could not be directly applied to the macroscopic modeling of deployable structures due to the lack of VE-VP continuum model. Liu et al. [51] proposed numerical homogenization strategies to calibrate material parameters for the transverse VE-VP behavior of unidirectional composites. However, the resulting homogenized constitutive models are essentially isotropic and thus insufficient to fully characterize the anisotropic behavior inherent to composites. To fill this gap, the authors have recently developed a continuum anisotropic VE-VP constitutive model specifically tailored for thin-ply composite laminates. The model has demonstrated its capability to capture the full spectrum of time-dependent and plastic behavior exhibited by high-strain composites used in space deployable structures throughout their service life [52]. Several related studies have been carried out to characterize the representative viscoelastic-viscoplastic response of composite materials [53–57]. However, a portion of the model parameters is difficult to measure directly through experiments, particularly those associated with the long-term viscoplastic behavior and anisotropic yield characteristics. A key limitation of phenomenological models is their lack of direct connection to the underlying physical mechanisms, which restricts their ability to offer meaningful insights into the microstructural origins of the observed macroscopic behavior. In contrast, a bottom-up multiscale modeling framework based on numerical homogenization provides a promising alternative for deriving lamina-level properties from the behavior of unidirectional yarns and the polymer matrix. This approach has the potential to reduce experimental demands while improving the predictive accuracy and physical relevance of the macroscopic model.

The present paper develops a comprehensive multiscale modeling framework to characterize the time-dependent and plastic responses of high-strain composites employed in deployable space structures. Constitutive VE-P models are formulated at three scales: an isotropic VE-P model is constructed for the polymer matrix, and two anisotropic VE-P models are developed for both unidirectional fiber yarns and woven composite laminae. The polymer matrix parameters are calibrated using experimental data from the literature. RVE models at the microscale and mesoscale are employed to determine the effective VE-P properties of the unidirectional yarns and woven laminae, respectively. To enable structural-scale simulations, user-defined material subroutines (UMAT)

are implemented to incorporate the anisotropic VE-P behavior of the composite lamina into finite element analyses. The multiscale predictions are validated against experimental measurements at the lamina level. Finally, the framework is applied at the macroscale to simulate the folding, stowage, deployment, and recovery processes of a thin-walled composite lenticular boom, capturing key phenomena such as shape recovery and permanent deformation.

The remaining content is organized as follows. Section 2 introduces the proposed multiscale modeling framework. Section 3 presents the three viscoelastic–plastic constitutive models developed in this paper, involving the polymer matrix, the unidirectional fiber yarn, and the woven composite lamina, respectively, along with their numerical implementations. Section 4 describes a two-scale numerical homogenization strategy for identifying the material parameters of the continuum constitutive models at different scales. Section 5 provides numerical case studies that validate the effectiveness of the proposed multiscale modeling framework through comparison with available experimental results. These include the mechanical behavior of the polymer matrix, the efficiency of the numerical homogenization scheme, and the simulation of column bending test responses based on the developed composite constitutive models and the homogenized material parameters. Section 6 applies the proposed framework to simulate the flattening-storage-deployment-recovery periods of a typical deployable structure, further demonstrating its capability in capturing the long-term performance of composite deployable structures during service. Finally, Section 7 concludes the paper.

2. Multiscale modeling framework

The time-dependent mechanical behavior of composite deployable structures during service primarily originates from the intrinsic viscosity and plasticity of the polymer matrix, while their anisotropic mechanical response arises from the unique micro- and meso-architectures of the materials. As illustrated in Fig. 1, a representative deployable structure-namely, a composite thin-walled lenticular tube-is constructed from a laminated structure composed of several layers of plain-weave fabric plies. The mesoscale image shown in Fig. 1 reveals that each fabric layer consists of fiber yarns woven into distinct patterns, forming a specific meso-architecture, with the remaining regions filled by the resin matrix. At the microscale, as observed in the corresponding microscale image, each fiber yarn comprises densely aligned unidirectional carbon fibers. Similar to the mesoscale configuration, the interstitial resin matrix at the microscale serves to maintain the stability and integrity of the microstructure. These hierarchical and architecturally distinct features at different length scales endow the composites with their anisotropic mechanical properties. Consequently, RVE models can be constructed based on the characteristic microstructural features at each scale. By performing numerical homogenization on the RVE models, one can extract the effective constitutive parameters for the higher-scale continuum, which are essential for the modeling, analysis, and design of composite deployable structures.

A multiscale modeling framework is developed for high-strain composite materials used in deployable structures through a two-step numerical homogenization strategy. In fact, as emphasized in previous studies, the key mechanical behaviors of composite deployable structures during service include stress relaxation during the storage period, residual deformation recovery after deployment, and permanent residual deformation [1,4]. A viscoelastic–plastic constitutive model is sufficient to capture these three essential mechanical responses [52]. Therefore, the mechanical behavior of the polymer matrix is described using an isotropic viscoelastic–plastic constitutive model, while the carbon fibers are assumed to exhibit linear orthotropic elastic behavior. In the first step of homogenization, a micro-RVE model for fiber yarn is constructed to determine the effective anisotropic viscoelastic–plastic constitutive parameters at the fiber yarn level. In the second step of homogenization, a meso-RVE model of a single ply plain-weave fabric is established, wherein both the anisotropic viscoelastic–plastic behavior of the unidirectional fiber yarns and the isotropic viscoelastic–plastic behavior of the resin matrix are incorporated. This step calculates the anisotropic viscoelastic–plastic constitutive parameters for the homogenized woven composite lamina. Subsequently, the macroscopic time-dependent mechanical response at the continuum level of the composite deployable structure is described by employing the Kirchhoff–Love plate theory in conjunction with classical laminate theory (CLT) in conjunction with the anisotropic viscoelastic–plastic constitutive model for woven composite lamina.

3. Viscoelastic–plastic constitutive model

Three nonlinear constitutive models are incorporated into the multiscale modeling strategy developed in this paper: an isotropic viscoelastic–plastic model for the polymer matrix, an anisotropic viscoelastic–plastic model for unidirectional fiber yarns, and an anisotropic viscoelastic–plastic model for the single-ply woven composite lamina. Under the infinitesimal strains, all three models adopt a common strain decomposition. Specifically, the total strain tensor $\boldsymbol{\varepsilon}$ is decomposed into a time-dependent viscoelastic component $\boldsymbol{\varepsilon}^{ve}$ and an irrecoverable plastic component $\boldsymbol{\varepsilon}^{p}$:

$$\boldsymbol{\varepsilon} = \boldsymbol{\varepsilon}^{ve} + \boldsymbol{\varepsilon}^{p} \tag{1}$$

The history of the viscoelastic strain tensor $\boldsymbol{\varepsilon}^{ve}(s)$ for $s \le t$ is related to the history of the Cauchy stress tensor $\boldsymbol{\sigma}(t)$ through a linear viscoelastic constitutive model expressed in the Boltzmann hereditary integral form:

$$\boldsymbol{\sigma}(t) = \int_0^t \boldsymbol{C}(t-s) : \frac{\partial \boldsymbol{\varepsilon}^{ve}(s)}{\partial s} ds \tag{2}$$

where $\boldsymbol{C}(t)$ denotes the fourth-order relaxation tensor. The plastic strain tensor $\boldsymbol{\varepsilon}^{p}$, which characterizes the material's permanent deformation, is governed by a flow rule:

$$\dot{\boldsymbol{\varepsilon}}^{p} = \dot{p}\frac{\partial H}{\partial \boldsymbol{\sigma}} = \dot{p}\boldsymbol{N} \tag{3}$$

Here, H denotes the plastic potential function, which also serves as the yield function under the associated flow rule adopted in this paper. The scalar variable p represents the equivalent plastic strain, defined as the norm of the plastic strain tensor consistent with the chosen yield criterion. The tensor N indicates the direction of plastic flow and is normal to the yield surface in principal stress space. The yield surface is defined as follows:

$$H = H(\sigma_{eq}, r) = 0 \tag{4}$$

In this context, σ_{eq} denotes the equivalent stress, defined as the norm of the Cauchy stress tensor consistent with the adopted yield criterion, and is conjugate to the equivalent plastic strain p. The scalar variable r represents the internal variable in scalar form, which characterizes the isotropic hardening behavior of the materials. For modeling simplicity, kinematic hardening effects are not considered in the present formulation. During plastic flow, Eq. (4) must be satisfied at all times, following the consistency condition. The above outlines the general framework of the viscoelastic–plastic constitutive model. In the following sections, the specific features and numerical implementations of the three constitutive models are described in detail.

3.1. Isotropic viscoelastic–plastic model for polymer matrix

The polymer matrix in composites exhibits isotropic mechanical behavior. The isotropic viscoelastic–plastic constitutive model presented in this section is primarily based on the work of Miled et al. [59]. The fourth-order relaxation tensor of the polymer, denoted as $\boldsymbol{C}^{iso}(t)$, can be decomposed as follows:

$$\boldsymbol{C}^{iso}(t) = 2G(t)\boldsymbol{I}^{dev} + 3K(t)\boldsymbol{I}^{vol} \tag{5}$$

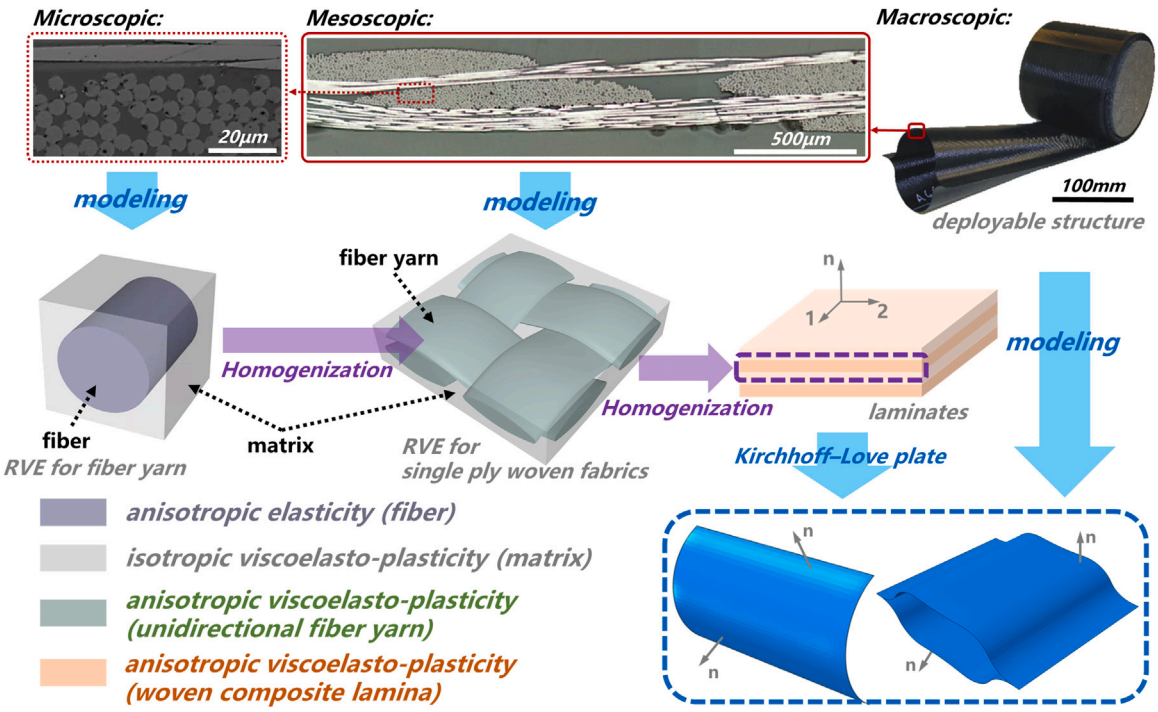

Fig. 1. Multiscale modeling concept of high-strain composites for deployable structures. (The microscale cross-section picture of the fiber yarn is modified from Hamillage et al. [17], the mesoscale cross-section picture of the fabrics is modified from Mallikarachchi [15], and the semi-deployed composite thin-walled lenticular tube (CTLT) shown at macroscale, modified from Block et al. [58]).

where $\boldsymbol{I}^{dev}$ and $\boldsymbol{I}^{vol}$ represent the deviatoric and volumetric fourth-order projection tensors, respectively. $G(t)$ and $K(t)$ denote the shear and bulk relaxation moduli, both expressed in the form of Prony series:

$$G(t) = G_\infty + \sum_{i=1}^{n} G_i e^{-t/g_i} \tag{6}$$

$$K(t) = K_\infty + \sum_{j=1}^{m} K_j e^{-t/k_j} \tag{7}$$

where $g_i (i = 1, \ldots, n)$ and $k_j (j = 1, \ldots, m)$ represent the shear and bulk relaxation times, respectively, while $G_i (i = 1, \ldots, n)$ and $K_j (j = 1, \ldots, m)$ are the corresponding relaxation moduli. G_∞ and K_∞ denote the long-term shear and bulk moduli, respectively. All these parameters are determined through experimental calibration. Substituting Eqs. (5), (6), and (7) into Eq. (2) results in the constitutive formulation of the viscoelastic response for the polymer matrix:

$$\boldsymbol{\sigma}_D(t) = 2G_\infty \boldsymbol{\varepsilon}_D^{ve}(t) + \sum_{i=1}^{n} \boldsymbol{\sigma}_{Di}(t) \tag{8}$$

$$\boldsymbol{\sigma}_H(t) = 3K_\infty \boldsymbol{\varepsilon}_H^{ve}(t) + \sum_{j=1}^{m} \boldsymbol{\sigma}_{Hj}(t) \tag{9}$$

where $\boldsymbol{\sigma}_D$ and $\boldsymbol{\sigma}_H$ denote the deviatoric and volumetric parts of the Cauchy stress tensor, respectively, and $\boldsymbol{\varepsilon}_D^{ve}$ and $\boldsymbol{\varepsilon}_H^{ve}$ represent the corresponding deviatoric and volumetric components of the strain tensor. $\boldsymbol{\sigma}_{Di}$ and $\boldsymbol{\sigma}_{Hj}$ are the viscous components associated with shear and volumetric relaxation, respectively:

$$\boldsymbol{\sigma}_{Di}(t) = 2G_i e^{-t/g_i} \int_0^t e^{s/g_i} \frac{\partial \boldsymbol{\varepsilon}_D^{ve}(s)}{\partial s} ds \tag{10}$$

$$\boldsymbol{\sigma}_{Hj}(t) = 3K_j e^{-t/k_j} \int_0^t e^{s/k_j} \frac{\partial \boldsymbol{\varepsilon}_H^{ve}(s)}{\partial s} ds \tag{11}$$

In the modeling framework developed in this paper, the plastic behavior of the polymer matrix is characterized using the J2 yield criterion. The expression of the yield function H^m is given as follows:

$$H^m = \sigma_{eq}^{J2} - R_0 - r \tag{12}$$

where R_0 denotes the yield strength of the polymer, and r represents the drag stress associated with isotropic hardening. Its expression is given by:

$$r = Bp^N \tag{13}$$

where B and N are hardening parameters determined through experimental calibration. The equivalent stress associated with the J2 yield criterion, denoted as σ_{eq}^{J2}, is expressed as:

$$\sigma_{eq}^{J2} = \sqrt{\frac{3}{2}\boldsymbol{\sigma}_D : \boldsymbol{\sigma}_D} \tag{14}$$

Therefore, by substituting Eq. (14) into Eq. (3), the plastic flow rule for the polymer matrix in the composites, can be obtained as follows:

$$\dot{\boldsymbol{\varepsilon}}^p = \frac{3}{2}\frac{\boldsymbol{\sigma}_D}{\sigma_{eq}^{J2}}\dot{p} \tag{15}$$

3.2. Anisotropic viscoelastic–plastic model for unidirectional fiber yarn

Due to its unique unidirectional microstructure, the fiber yarn exhibits transverse isotropic behavior. The constitutive model presented in this section is used to describe the mechanical behavior of the fiber yarn continuum. The expression for the fourth-order relaxation tensor $\boldsymbol{C}^{UD}(t)$ of the fiber yarn in the form of a Prony series is given as follows:

$$\boldsymbol{C}^{UD}(t) = \boldsymbol{C}_\infty^{UD} + \sum_{i=1}^{n} \boldsymbol{C}_i^{UD} e^{-t/\rho_i^{UD}} \tag{16}$$

where ρ_i^{UD} denotes the relaxation time, $\boldsymbol{C}_i^{UD} (i = 1, \ldots, n)$ are the corresponding moduli, and $\boldsymbol{C}_\infty^{UD}$ represents the long-term modulus. The above form is sufficient to describe the anisotropic mechanical response of fiber yarn in the viscoelastic part. These parameters are obtained from the first step of the numerical homogenization. Substituting Eq. (16) into Eq. (2) gives the viscoelastic part of the constitutive model for the fiber yarn as follows:

$$\boldsymbol{\sigma}(t) = \boldsymbol{C}_\infty^{UD} : \boldsymbol{\varepsilon}^{ve}(t) + \sum_{i=1}^{n} \boldsymbol{C}_i^{UD} : \boldsymbol{q}_i(t) \tag{17}$$

where

$$\boldsymbol{q}_i(t) = \int_0^t e^{-(t-s)/\rho_i} \frac{\partial \boldsymbol{\varepsilon}^{ve}(s)}{\partial s} ds \tag{18}$$

The above expression is consistent with the constitutive model for the fiber yarn used in the two-step homogenization scheme based on viscoelastic models, as presented by Kwok et al. [6,17]. The present paper extends this model to viscoelastic–plastic behavior to accommodate the permanent deformations widely observed in experiments on high-strain composites for deployable structures [7,9].

The key to modeling the plastic part in the constitutive model is to accurately describe the anisotropic yielding and plastic flow behavior of the fiber yarn. Hill [60] presented the general form of the 3D fiber composites yield function H as follows:

$$\begin{aligned} 2H(\sigma_{ij}) =& a_{11}\sigma_{11}^2 + a_{22}\sigma_{22}^2 + a_{33}\sigma_{33}^2 + 2a_{12}\sigma_{11}\sigma_{22} + 2a_{13}\sigma_{11}\sigma_{33} + 2a_{23}\sigma_{22}\sigma_{33} \\ &+ 2a_{44}\sigma_{23}^2 + 2a_{55}\sigma_{13}^2 + 2a_{66}\sigma_{12}^2 \end{aligned} \tag{19}$$

where σ_{ij} denotes the components of the Cauchy stress tensor, and a_{ij} represents the anisotropic parameters. When $a_{11} = a_{22} = a_{33} = 2/3$, $a_{12} = a_{13} = a_{23} = -1/3$, and $a_{44} = a_{55} = a_{66} = 1$, the J2 yield function from Section 3.1 is obtained. Experimental investigations indicate that unidirectional fiber composites exhibit almost no yielding or plastic flow behavior when loaded along the fiber direction, but show the most significant yielding and plastic flow behavior when loaded perpendicular to the fiber direction [61,62]. Therefore, it is reasonable to assume that the stress in the fiber direction (1-direction) does not affect the value of the yield function for the fiber yarn, that is:

$$\varepsilon_{11}^p \equiv 0 \tag{20}$$

Additionally, considering the plane perpendicular to the fiber direction (2–3 plane) as an isotropic plane, the yield function in Eq. (19) can be modified to H^{UD} as follows:

$$2H^{UD}(\sigma_{ij}) = \left(\sigma_{22} - \sigma_{33}\right)^2 + 2a_{44}\sigma_{23}^2 + 2a_{66}\left(\sigma_{13}^2 + \sigma_{12}^2\right) \tag{21}$$

The above expression is similar to the results derived by Chen and Sun [63], with two anisotropic parameters, a_{44} and a_{66}, that need to be calibrated. Considering the plane stress state, Eq. (21) leads to:

$$2H^{UD}(\sigma_{ij}) = \sigma_{22}^2 + 2a_{66}\sigma_{12}^2 \tag{22}$$

The above expression represents the classical one-parameter plastic potential function for a single ply unidirectional composite lamina [64]. The expression for the equivalent stress, σ_{eq}, is given as:

$$\sigma_{eq} = \sqrt{3H(\sigma_{ij})} \tag{23}$$

By combining Eq. (23) and (21), the equivalent stress for fiber yarn σ_{eq}^{UD} following is obtained:

$$\sigma_{eq}^{UD} = \sqrt{\frac{3}{2}\left[\left(\sigma_{22} - \sigma_{33}\right)^2 + 2a_{44}\sigma_{23}^2 + 2a_{66}\left(\sigma_{13}^2 + \sigma_{12}^2\right)\right]} \tag{24}$$

Similar to the polymer matrix, the expression for the yield function of the fiber yarn is given as:

$$H^{UD} = \sigma_{eq}^{UD} - \left(\alpha_0 + hp^m\right) = 0 \tag{25}$$

where α_0 represents the initial drag stress, and h and m are hardening parameters obtained from the first step of the numerical homogenization scheme. The expression for the equivalent stress of the fiber yarn, σ_{eq}^{UD}, in Eq. (24) can also be written in the following form:

$$\sigma_{eq}^{UD} = \sqrt{\frac{3}{2}\boldsymbol{\sigma} : \boldsymbol{M}^{UD} : \boldsymbol{\sigma}} \tag{26}$$

where $\boldsymbol{M}^{UD}$ is the fourth-order anisotropic parameter tensor, and its expression in Voigt notation is given as:

$$\boldsymbol{M}^{UD} = \begin{pmatrix} 0 & 0 & 0 & 0 & 0 & 0 \\ 0 & 1 & -1 & 0 & 0 & 0 \\ 0 & -1 & 1 & 0 & 0 & 0 \\ 0 & 0 & 0 & 2a_{44} & 0 & 0 \\ 0 & 0 & 0 & 0 & 2a_{66} & 0 \\ 0 & 0 & 0 & 0 & 0 & 2a_{66} \end{pmatrix} \tag{27}$$

By substituting Eq. (26) into Eq. (3), the plastic flow rule for the fiber yarn is obtained as follows:

$$\dot{\boldsymbol{\varepsilon}}^p = \frac{3}{2}\frac{\boldsymbol{M}^{UD} : \boldsymbol{\sigma}}{\sigma_{eq}^{UD}}\dot{p} \tag{28}$$

3.3. Anisotropic viscoelastic–plastic model for woven composite lamina

Classical laminate theory is widely used in the modeling of composite thin-walled deployable structures. Therefore, a plane stress composite viscoelastic–plastic constitutive model is required to describe the mechanical behavior of single-ply woven composite lamina. In recent work, the authors developed a viscoelastic-viscoplastic constitutive model framework for woven composite lamina [52], which, when excluding the overstress item, can degrade to the viscoelastic–plastic constitutive model for single-ply woven composite lamina required for this paper. The viscoelastic part of the lamina constitutive model adopts the plane stress forms of Eqs. (16), (17), and (18), where the material parameters in the fourth-order relaxation tensor $\boldsymbol{C}^{PW}$ for the woven composite lamina are obtained through the second step of the numerical homogenization scheme. Experimental investigations indicate that woven composites exhibit almost no yielding or plastic flow behavior when loaded in the fiber yarn direction (warp or weft direction), while they exhibit the most significant plastic flow behavior when loaded in the 45° direction [65]. Therefore, it is reasonable to assume that the stress in the fiber yarn direction (1,2-direction) does not affect the value of the yield function for the woven composite lamina, that is:

$$\varepsilon_{11}^p \equiv 0 \quad and \quad \varepsilon_{22}^p \equiv 0 \tag{29}$$

Considering the plane stress state, the yield function for the woven composite lamina is given as:

$$2H^{PW}(\sigma_{ij}) = 2\sigma_{12}^2 \tag{30}$$

By substituting Eq. (30) into Eq. (23), the equivalent stress σ_{eq}^{PW} for the woven composite lamina, is obtained as:

$$\sigma_{eq}^{PW} = \sqrt{\frac{3}{2}\left(2\sigma_{12}^2\right)} \tag{31}$$

By substituting Eq. (31) into Eq. (3), the plastic flow rule for the woven composite lamina, is obtained as:

$$\begin{pmatrix} \dot{\varepsilon}_{11}^p \\ \dot{\varepsilon}_{22}^p \\ \dot{\gamma}_{12}^p \end{pmatrix} = \frac{3}{2}\frac{\dot{p}}{\sigma_{eq}^{PW}} \begin{pmatrix} 0 & 0 & 0 \\ 0 & 0 & 0 \\ 0 & 0 & 2 \end{pmatrix} \begin{pmatrix} \sigma_{11} \\ \sigma_{22} \\ \sigma_{12} \end{pmatrix} \tag{32}$$

The corresponding yield function is:

$$H^{PW} = \sigma_{eq}^{PW} - \left(r_0 + bp^n\right) = 0 \tag{33}$$

Here, r_0 denotes the initial value of the drag stress for the lamina, while b and n are hardening parameters obtained from the second-step numerical homogenization process. The proposed constitutive model for the woven composite lamina exhibits general applicability and effectively captures the mechanical behavior of single-ply composite lamina. Detailed validation of the model's effectiveness can be found in the authors' recent work [52].

3.4. Numerical implementation

Despite three viscoelastic–plastic constitutive models are incorporated into the multiscale analysis presented in this paper, a general numerical implementation scheme applicable to all three can still be formulated. Compared with previous modeling efforts that focused on time-dependent mechanical behavior of thin-walled composite deployable structures based on viscoelastic models, the primary advancement in the present work lies in coupling plasticity with the viscoelastic framework. This is achieved through a validated two-step numerical solution strategy based on the return mapping algorithm. The objective of the numerical scheme is, given the known stress $\boldsymbol{\sigma}(t_n)$, strain $\boldsymbol{\epsilon}(t_n)$, time increment Δt, and corresponding strain increment $\Delta\boldsymbol{\epsilon}$ over the interval $[t_n, t_{n+1}]$, to compute the correct stress increment $\Delta\boldsymbol{\sigma}$ for updating the stress to $\boldsymbol{\sigma}(t_{n+1})$. The key to this strategy involves deriving a stress update formulation for the viscoelastic model in the total strain increment form (viscoelastic predictor), followed by a return mapping algorithm for plastic correction (plastic corrector). The "viscoelastic predictor" is:

$$\boldsymbol{\sigma}^{pred}(t_{n+1}) = \boldsymbol{\sigma}(t_n) + \tilde{\boldsymbol{C}} : \Delta\boldsymbol{\epsilon} + \sum_{i=1}^{n} \left(e^{-\Delta t/\rho_i} - 1\right) \boldsymbol{C}_i : \boldsymbol{q}_i(t_n) \tag{34}$$

where:

$$\tilde{\boldsymbol{C}} = \boldsymbol{C}_\infty + \sum_{i=1}^{n} \boldsymbol{C}_i \frac{\rho_i}{\Delta t}\left(1 - e^{-\Delta t/\rho_i}\right) \tag{35}$$

$$\boldsymbol{q}_i(t_{n+1}) = e^{-\Delta t/\rho_i}\boldsymbol{q}_i(t_n) + \frac{\rho_i}{\Delta t}\left(1 - e^{-\Delta t/\rho_i}\right)\Delta\boldsymbol{\epsilon}^{ve} \tag{36}$$

where $\tilde{\boldsymbol{C}}$ is the fourth-order incremental relaxation tensor, and $\boldsymbol{q}_i$ are updated recursively. When $f\left(\boldsymbol{\sigma}^{pred}(t_{n+1})\right) \le 0$, we have:

$$\boldsymbol{\sigma}(t_{n+1}) = \boldsymbol{\sigma}^{pred}(t_{n+1}) \tag{37}$$

Otherwise, the plastic correction procedure is executed:

$$\boldsymbol{\sigma}(t_{n+1}) = \boldsymbol{\sigma}^{pred}(t_{n+1}) - \tilde{\boldsymbol{C}} : \Delta\boldsymbol{\epsilon}^{p} \tag{38}$$

The key in the above formulation lies in the computation of $\Delta\boldsymbol{\epsilon}^p$, which can be obtained from Eq. (3) as:

$$\Delta\boldsymbol{\epsilon}^{p} = \Delta p\boldsymbol{N} \tag{39}$$

The Newton–Raphson iteration method is used over the time interval $[t_n, t_{n+1}]$ to solve for Δp in Eq. (39). According to the consistency condition, Eq. (3) holds throughout the plastic flow process. Therefore, a first-order Taylor expansion of Eq. (3) is applied as follows:

$$H + \frac{\partial H}{\partial \Delta p}d\Delta p + \frac{\partial H}{\partial r}dr = 0 \tag{40}$$

The Newton–Raphson iteration scheme can be constructed from the above equation:

$$RES = H = 0 \tag{41}$$

$$d\Delta p = \frac{H + \partial H/\partial r}{\partial H/\partial \Delta p} \tag{42}$$

$$\Delta p^{(k+1)} = \Delta p^{(k)} + d\Delta p \tag{43}$$

The numerical scheme presented above achieves satisfactory convergence, with a strain increment of 1×10^{-3}, local convergence can be achieved within four iterations, and more detailed derivations and implementation procedures can be found in the author's recent work [52]. The three constitutive models included in this section, namely, the 3D isotropic viscoelastic–plastic model for the polymer matrix, the 3D anisotropic viscoelastic–plastic model for fiber yarn, and the plane stress anisotropic model for woven composite lamina, have all been implemented based on the numerical scheme in Section 3.4 through user material subroutines (UMAT) in the commercial finite element code ABAQUS [66].

4. Two-step numerical homogenization

Section 3 establishes the viscoelastic–plastic constitutive models for continua at different scales, which essentially represent a mapping relation $\mathbb{F}^{continua}$, that is, calculating the stress response given the strain (or calculating the strain response given the stress):

$$\boldsymbol{\sigma} = \mathbb{F}^{continua}\left(\boldsymbol{\epsilon}, x_1, x_2, \ldots\right) \tag{44}$$

where $x_1, x_2, \ldots$ are the constitutive model parameters to be determined. For the RVE model of two-phase or multi-phase materials, a virtual experiment $\mathbb{F}^{RVE}$ (usually finite element analysis) is conducted. By applying macroscopic strain $\bar{\boldsymbol{\epsilon}}$, the macroscopic stress response $\bar{\boldsymbol{\sigma}}$ of the RVE can be obtained as follows:

$$\bar{\boldsymbol{\sigma}} = \mathbb{F}^{RVE}\left(\bar{\boldsymbol{\epsilon}}\right) \tag{45}$$

where:

$$\bar{\boldsymbol{\sigma}} = \frac{1}{V}\int_{\bar{V}} \boldsymbol{\sigma}(x, y, z)dV \tag{46}$$

$$\bar{\boldsymbol{\epsilon}} = \frac{1}{V}\int_{\bar{V}} \boldsymbol{\epsilon}(x, y, z)dV \tag{47}$$

The purpose of numerical homogenization is to obtain a set of determined constitutive model parameters $x_1, x_2, \ldots$, such that under the same conditions, the response of the continuum model is the same as the macroscopic response of the RVE model, that is:

$$\forall\bar{\boldsymbol{\epsilon}}, \quad \mathbb{F}^{continua}\left(\bar{\boldsymbol{\epsilon}}, x_1, x_2, \ldots\right) = \mathbb{F}^{RVE}\left(\bar{\boldsymbol{\epsilon}}\right) \tag{48}$$

In this section, a two-step numerical homogenization strategy is developed to determine the effective viscoelastic–plastic behavior of a continuous single-ply lamina. The first-step homogenization is carried out at the microscale, where virtual tests are conducted on the fiber yarn RVE model (Fig. 2(a)) to obtain the viscoelastic–plastic constitutive parameters of the fiber yarn. The second-step homogenization is performed at the mesoscale, where virtual tests on the plain-weave fabric RVE model (Fig. 2(b)) are used to further determine the viscoelastic–plastic constitutive parameters of the single-ply woven lamina. Fig. 2(c) illustrates the workflow of the proposed method. First, experimental data for the fiber and polymer matrix are collected and used to calibrate their respective material parameters. The fiber is modeled as a transversely isotropic elastic material and defined directly using the ABAQUS built-in material model. In contrast, the polymer matrix is modeled as a three-dimensional (3D) isotropic VE-P material, implemented via a user-defined UMAT. Next, the micro-RVE is generated and used to compute the effective VE-P properties of the unidirectional fiber yarn. These properties are then incorporated into a 3D anisotropic VEP UMAT to represent the behavior of the yarns. In the subsequent meso-RVE analyses, the fiber yarns are modeled using the 3D anisotropic VE-P UMAT, while the matrix continues to be modeled using the isotropic VE-P UMAT. These simulations provide the effective VE-P properties of the woven lamina. Finally, these properties are implemented in a plane-stress anisotropic VE-P UMAT to define the behavior of each lamina. The composite layup is defined using the *Composite Shell method within the ABAQUS built-in function to simulate the structural response of generalized shell components.

Experimental data on composites reported by Hamillage et al. [10] are used to validate the effectiveness of the method developed in this paper. The thin-ply composite laminates is fabricated using M30S carbon fibers (Toray Industries) and PMT-F7 epoxy resin (Patz Materials and Technologies), and the modeling parameters for the RVE models are therefore adopted from studies on the same composite system [17], as listed in Table 1.

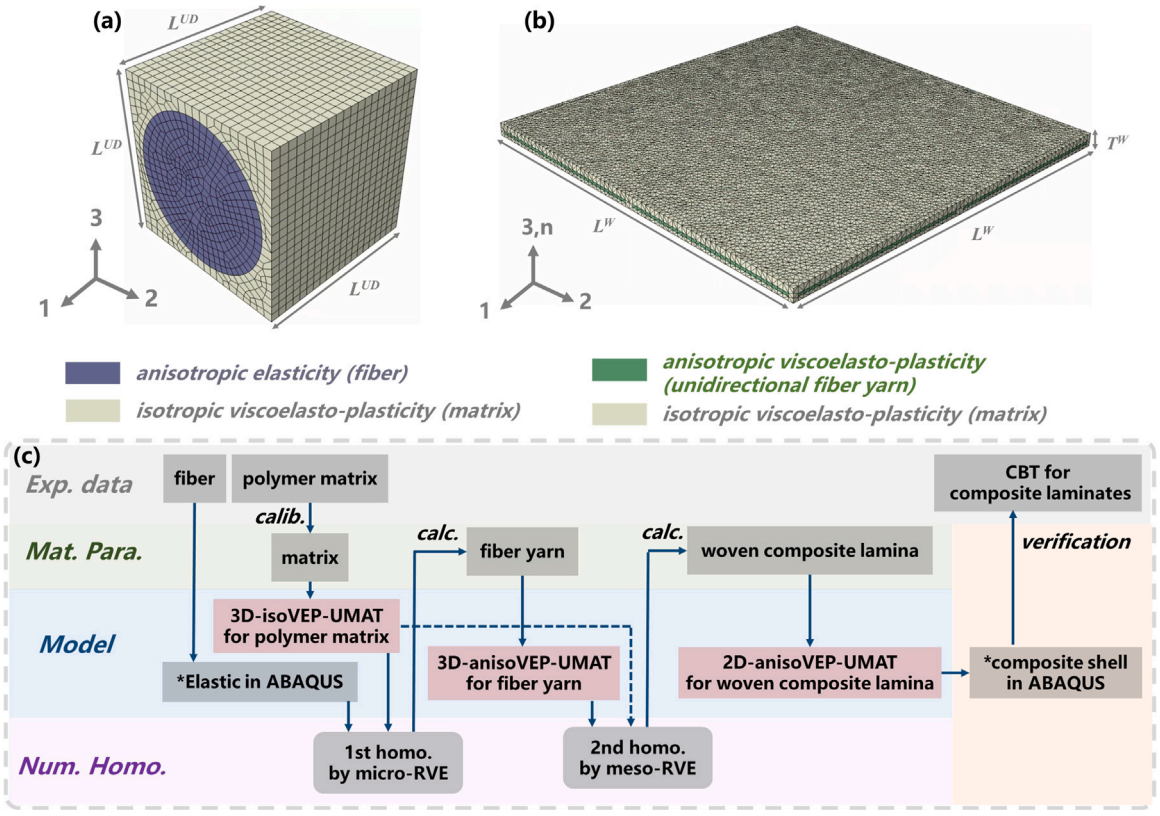

Fig. 2. Finite element models: (**a**) microscale unidirectional RVE model for fiber yarn (micro-RVE), (**b**) mesoscale plain-weave RVE model for fabric lamina (meso-RVE), (**c**) schematic representation of two-step numerical homogenization.

Table 1
Modeling parameters of laminate [10,17].

Properties	Values, Unit
Number of layers	3
Laminate thickness	0.201, mm
Fiber vol. frac. of fiber yarn	62%
Fiber vol. frac. of laminate	52%
Fiber yarn vol. frac. of laminate	83%

4.1. Microscale fiber yarn model

Fiber yarns are essentially a type of unidirectional composite, and therefore, the unidirectional micro-RVE model can be employed to simulate their mechanical response. As shown in Fig. 2(a), the fiber yarn is modeled as a cylindrical fiber embedded in a cubic polymer matrix. This micro-RVE configuration is sufficient to capture the microstructural characteristics of real-world fiber yarns. The M30S carbon fiber is assumed to exhibit transverse isotropic elasticity (purple region in Fig. 2(a)), with the isotropic plane in the 2–3 direction. The corresponding material parameters are listed in Table A.1 in the Appendix. The PMT-F7 epoxy matrix is modeled using an isotropic viscoelastic–plastic model (gray region in Fig. 2(a)), whose parameters are obtained from experimental data fitting; specific values (Table A.3) and fitting procedures are provided in the Appendix. A 3D isotropic UMAT was developed and implemented to simulate the VE-P behavior of the polymer matrix. The side length of the unidirectional micro-RVE model, L^{UD}, is 1 μm, and the fiber radius is set to 0.44 μm to match the fiber volume fraction of the yarn as listed in Table 1. The micro-RVE model is meshed using 11380 three-dimensional hexahedral elements (C3D8 in ABAQUS) for mesh generation to achieve a mesh-independent solution. Periodic boundary conditions (PBCs) were properly imposed to ensure the translational symmetry of the RVE model. Specifically, all pairs of nodes located at corresponding positions on each pair of opposite faces of the RVE were constrained to a common reference point using *Equation constraints in ABAQUS. This formulation enforces that, under arbitrary loading conditions, the relative displacement between paired nodes on opposite faces is consistent with the prescribed macroscopic strain of the RVE. A more detailed description of the implementation procedure can be found in the authors' previous work. [16,27,67].

In the first-step homogenization, virtual tests are conducted on the unidirectional micro-RVE model to determine the material parameters of the anisotropic viscoelastic–plastic constitutive model for fiber yarn described in Section 3.2. Two types of virtual tests are performed to calibrate the viscoelastic and plastic parts of the model separately. First, four constant macroscopic strain histories ε^{cst} are applied to the unidirectional micro-RVE to obtain the corresponding macroscopic stress relaxation responses, from which the time-dependent evolution of each component of the fourth-order relaxation tensor can be calculated, as shown in Eq. (16). This process corresponds to a static viscoelastic analysis, which can be performed in ABAQUS using the *Static General step in ABAQUS. The obtained time-dependent evolution data of relaxation tensor components are then fitted using a Prony series to determine the viscoelastic parameters of the fiber yarns. It is important to note that during the calibration of the viscoelastic part, the applied macroscopic strain histories must be sufficiently small to prevent yielding of the polymer matrix. For the plastic parameters, uniaxial macroscopic strain loading with the ramp mode is applied along different strain components on the unidirectional micro-RVE, with all other reference point degrees of freedom kept free. The corresponding macroscopic stress responses are recorded, and equivalent stress-equivalent plastic strain curves in different directions are computed. To capture the yielding and plastic deformation behavior of the model, the *Static General step in the ABAQUS solver is employed. A master curve of equivalent stress versus equivalent plastic strain is derived using the yield function and fitted with a hardening law to extract the plastic material parameters.

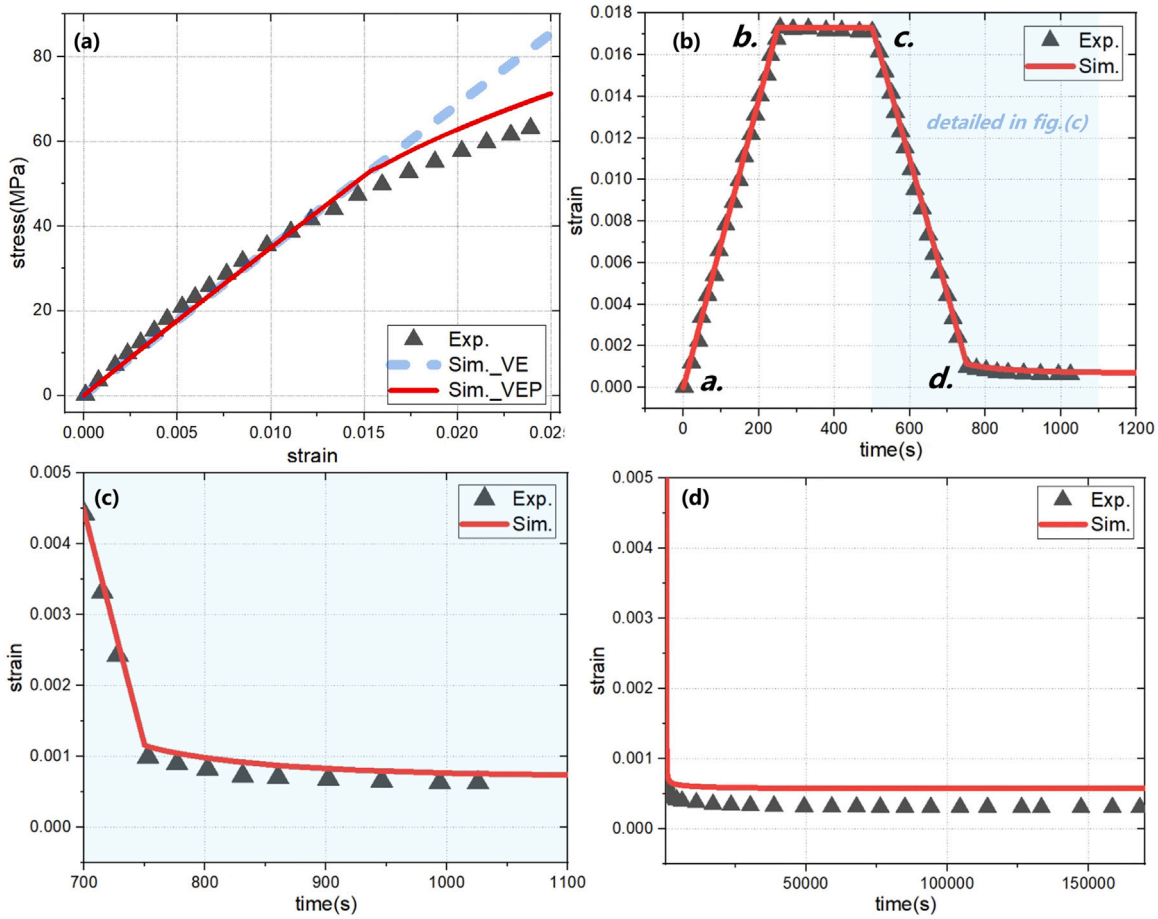

Fig. 3. Simulated results of PMT-F7 polymer, the experiments by Hamillage et al. [10] are shown for comparison: (**a**) stress–strain curves, simulated results by viscoelastic model are shown for comparison, (**b**) strain history during loading, relaxation, unloading, and initial recovery periods, (**c**) detailed strain history during unloading and initial recovery periods, (**d**) strain history during long-term recovery period.

The detailed procedure for the first-step numerical homogenization is provided in the Appendix.

4.2. Mesoscale woven lamina model

Based on the meso-architecture of the composite fabric, a single-ply plain-weave fabric lamina meso-RVE model was established as shown in Fig. 2(b). The plain-weave pattern of the model was generated using the open-source textile modeling software TexGen [68]. The fiber yarns are modeled as anisotropic viscoelasto-plasticity (green regions in Fig. 2(b)), with material parameters obtained from the first-step numerical homogenization process described in Section 4.1, as listed in Table A.4 of the Appendix. The PMT-F7 epoxy resin matrix is modeled as isotropic viscoelasto-plasticity (gray regions in Fig. 2(b)), consistent with Section 4.1. The side length of the meso-RVE model L^w is 6.675 mm, and the thickness T^w is 0.2 mm. The cross-section of the fiber yarns is assumed to be rectangular, with a width of 3.164 mm and a height of 0.05 mm. The geometric parameters of the meso-RVE model satisfy the fiber volume fraction requirements of the laminates, as listed in Table 1. The plain-weave meso-RVE model is meshed with 192924 three-dimensional tetrahedral elements (C3D4 in ABAQUS) to achieve a mesh-independent solution. The degrees of freedom of the opposing surface nodes are constrained to the reference point, and periodic boundary conditions (PBC) are applied. The deformation in the thickness direction of the woven meso-RVE model is restricted to conform to the Kirchhoff–Love assumption. The homogenization calculation of meso-RVE is also based on the *Static General step in ABAQUS.

In the second-step numerical homogenization, virtual tests are performed on the plain-weave meso-RVE model to determine the material parameters of the anisotropic viscoelastic–plastic constitutive model for woven composite lamina described in Section 3.3. Similar to the first-step homogenization process in Section 4.1, two types of virtual tests, stress relaxation and uniaxial tension, are conducted on the plain-weave meso-RVE model to calibrate the viscoelastic and plastic material parameters, respectively. The detailed procedure of the second-step numerical homogenization is provided in the Appendix. It is worth noting that in the composite deployable structures community, woven RVE models at mesoscale are commonly employed to directly compute the laminate stiffness matrix – the ABD matrix, or its stowage time-dependent counterpart – thereby defining the stiffness behavior of homogenized laminates [6,17,21]. While this approach is effective for both elastic and viscoelastic analyses, it becomes unsuitable for plasticity modeling, as plastic constitutive laws rely on stress-based yield criteria and flow rules. A more general and robust strategy involves assuming an anisotropic constitutive model at the lamina level, using RVE analyses to extract the required single-ply constitutive parameters via a second-step numerical homogenization, and subsequently applying classical laminate theory to evaluate the response of the Kirchhoff plate at each incremental step. This multiscale approach is broadly applicable to both viscoelastic and plastic models. The strategy is referred to by Hamillage et al. [69] as the ply homogenization method, and its effectiveness has been demonstrated in the numerical homogenization of viscoelastic models.

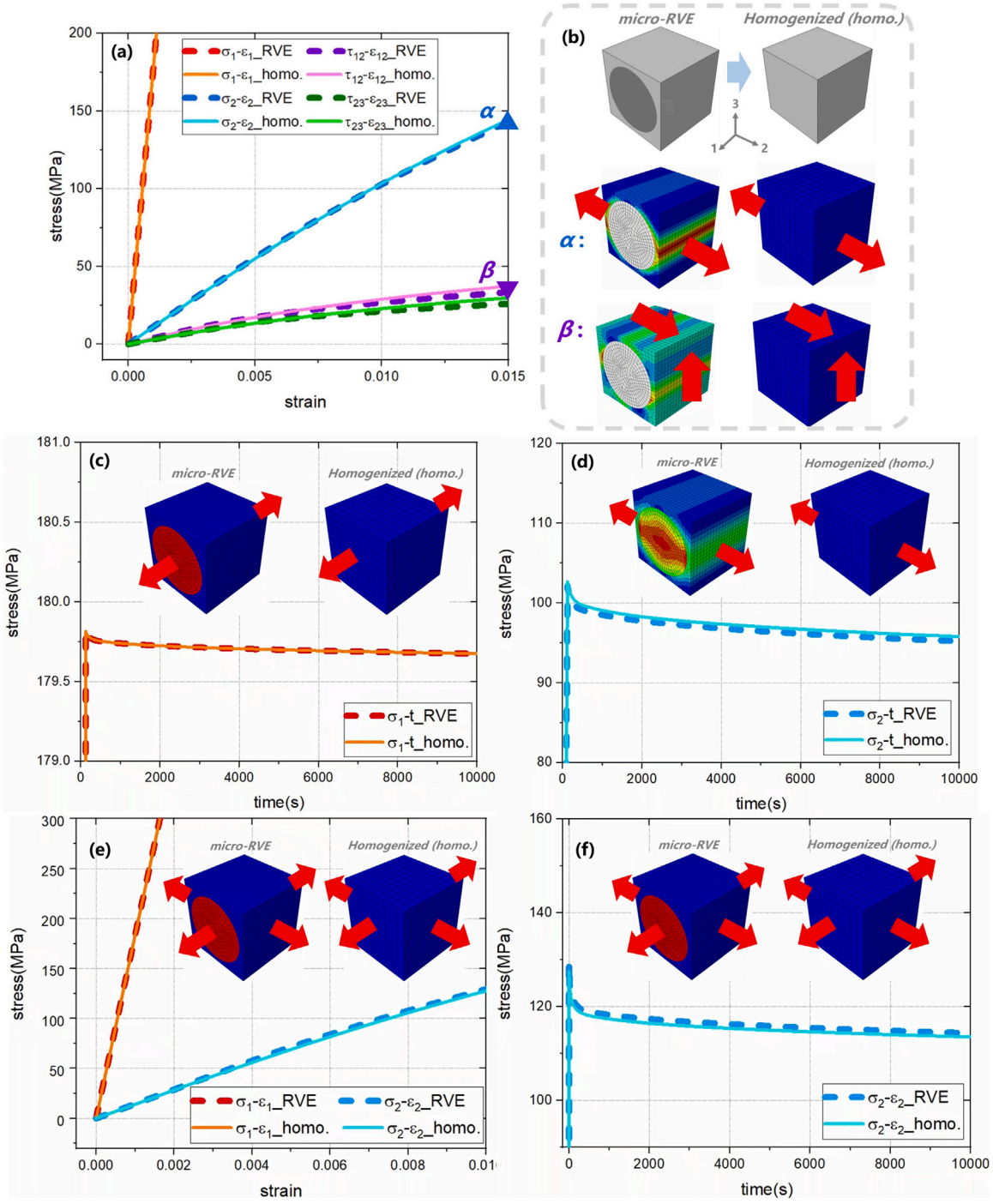

Fig. 4. Numerical homogenization of unidirectional micro-RVE model for fiber yarn: (**a**) stress–strain responses under simple loading conditions, (**b**) visualization, and distribution of equivalent plastic strain for micro-RVE and the homogenized model are shown, (**c**) relaxation response under constant displacement in 1-direction, (**d**) relaxation response under constant displacement in 2-direction, (**e**) stress–strain responses under multi-axial loading conditions, (**f**) relaxation responses under multi-axial loading conditions, and distribution of maximum principal stress for micro-RVE and the homogenized model are shown above.

5. Results and discussion

5.1. Mechanical response modeling for PMT-F7 polymer

The experimental data of PMT-F7 epoxy resin are derived from the systematic experimental investigations conducted by Hamillage et al. [10], and the time-dependent mechanical behavior of the PMT-F7 polymer is described using the constitutive model in Section 3.1. The viscoelastic material parameters are obtained from the previous work of Hamillage et al. [69], while the plastic parameters are calibrated from stress–strain curves (details are provided in the Appendix), and the material parameters are listed in Table A.3 in the Appendix. A uniaxial tensile finite element simulation of PMT-F7 epoxy resin was conducted with a strain rate of 0.01%/s, consistent with the experiment. The simulation calculated stress–strain curve (red solid line) is shown in Fig. 3(a) and agrees well with the experimental observations (black triangle dots). Under the same conditions, the stress–strain curve of PMT-F7 polymer based on the viscoelastic constitutive model (blue dashed line) is also presented in Fig. 3(a) for comparison. It can be observed that both constitutive models show good agreement with the

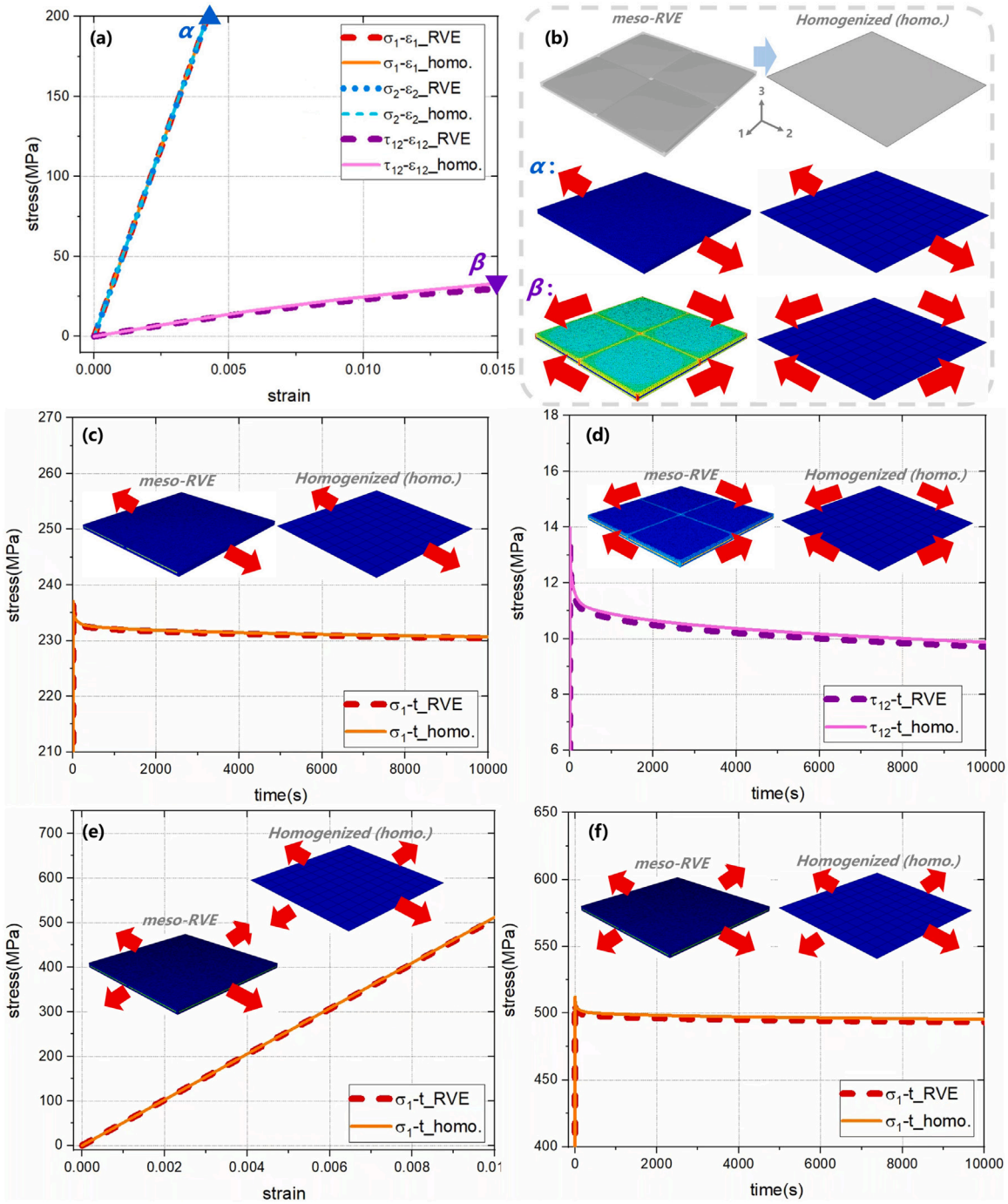

Fig. 5. Numerical homogenization of plain-weave meso-RVE model for fabric lamina: (**a**) stress–strain responses under simple loading conditions, (**b**) visualization, and distribution of equivalent plastic strain for meso-RVE and the homogenized model are shown, (**c**) relaxation response under constant displacement in 1-direction, (**d**) relaxation response under constant displacement in shear direction, (**e**) stress–strain response under multi-axial loading conditions, (**f**) relaxation response under multi-axial loading conditions, and distribution of maximum principal stress for meso-RVE and the homogenized model are shown above.

experimental observations before yielding, while the viscoelastic model deviates from the experimental data at higher strain levels.

It should be acknowledged that the constitutive model naturally captures the stress–strain behavior, as the stress–strain curve data are incorporated into the calibration of the material parameters. Therefore, a finite element simulation of the uniaxial relaxation-recovery test of PMT-F7 epoxy resin was conducted and compared with experimental data to verify the effectiveness of the modeling. Relaxation-recovery test data were not included in the constitutive parameter calibration process for PMT-F7 epoxy resin. Fig. 3(b) presents the strain history from the finite element simulation (red line) and experimental observations (black triangle dot). The PMT-F7 polymer is loaded to a specified strain level ($a.-b.$), which corresponds to the folding condition of deployable structures. Subsequently, the materials undergo a short storage period ($b.-c.$), during which stress relaxation occurs (the stress history was not provided in the experiment data). The material is then unloaded to a constraint-free state ($c.-d.$), and significant residual strain can be observed at point d. The history after point $d.$ is referred to as the recovery period, during which part of the residual deformation recovers and part remains as permanent deformation. The details of

the strain history during the recovery period are shown in Fig. 3(c), where the strain history captured by the finite element simulation agrees well with the test data, validating the effectiveness of the PMT-F7 constitutive model and its material parameters. The long-term strain recovery curve is shown in Fig. 3(d), where it can be seen that the finite element simulation overestimates the residual deformation of the polymer, indicating that the predictive capability of the constitutive model for long-term recovery behavior requires further improvement. A highly plausible explanation is that the viscoelastic–plastic constitutive model adopted in this paper attributes an excessive portion of the nonlinear stress–strain behavior of the PMT-F7 resin to plastic deformation, which leads to an overestimation of the plastic strain. A potential improvement, therefore, is to employ a nonlinear viscoelastic–plastic constitutive formulation to fit the stress–strain response, which may enable more accurate predictions of the long-term recovery behavior. This will be explored in future work.

5.2. Two-step numerical homogenization

Figs. 4(a), (c), (d), (e), and (f) show the comparison between the homogenized continuous constitutive model of the fiber yarn and the unidirectional micro-RVE about the stress–strain and stress relaxation responses. It can be seen that the continuous constitutive model completely reproduces the stress–strain and stress relaxation behavior of the micro-RVE, indicating that the numerical homogenization process has obtained the correct material parameters for the fiber yarn. It is also observed in Fig. 4(a) that the stress–strain curve in the fiber direction (1-direction in Fig. 4(b)) calculated by the micro-RVE exhibits linear characteristics, which further supports the reasonableness of the assumptions adopted in Section 3.2 regarding the mathematical form of the yield function for the fiber yarn. In particular, the multi-axis loading simulated results shown in Figs. 4(e) and (f) further verify the effectiveness and universality of the numerical homogenization process and parameter identification.

Figs. 5(a), (c), (d), (e), and (f) show the comparison between the homogenized continuous constitutive model of the single-ply woven composite lamina and the plain-weave meso-RVE about the stress–strain and stress relaxation responses. It can be seen that the continuous constitutive model completely reproduces the stress–strain and stress relaxation behavior of the meso-RVE, indicating that the numerical homogenization process has obtained the correct material parameters for the single-ply woven composite lamina. It is observed in Fig. 5(a) that the plain-weave meso-RVE model accurately captures the unique anisotropic mechanical behavior of woven composites, that is, the stress–strain curves in the warp and weft directions (1 and 2 directions in Fig. 5(b)) exhibit linear characteristics, while the most significant nonlinear behavior occurs in the shear direction. In particular, the multi-axis loading simulated results shown in Figs. 5(e) and (f) further verify the effectiveness and universality of the numerical homogenization process and parameter identification.

The yield surface and subsequent yield surface evolution on the σ_{11}–σ_{12} plane, computed from the plain-weave meso-RVE model, are shown in Fig. 6 (blue dashed lines with triangular markers). For comparison, the results obtained from the homogenized constitutive model are also presented (red lines in Fig. 6). It is worth noting that the present composite modeling framework assumes symmetric tensile and compressive responses. Therefore, only the first quadrant of the yield and subsequent yield surfaces are illustrated in Fig. 6. Furthermore, due to the consistent mechanical behavior in the warp and weft directions of the woven composite lamina, the yield surface and elastic domain of the homogenized model can be represented by an area enclosed between a pair of infinitely extended parallel planes in the plane stress space (red lines in Fig. 6), as detailed in our previous work [52]. As illustrated in Fig. 6, the yield surface predicted by the meso-RVE model (blue dashed lines with triangular markers) closely agrees with that obtained from the homogenized continuum model (red line), indicating consistency between the two modeling approaches. The resulting yield surface shape suggests that the yielding and plastic flow behavior of the woven composite laminate is largely insensitive to stresses along the warp and weft directions, but is predominantly governed by the in-plane shear stress. This observation aligns with the continuum modeling assumption adopted in Section 3.3 for the woven composite lamina.

The in-plane shear mechanical responses of the woven composite laminate meso-RVE model with different fiber yarn volume fractions are shown in Fig. 7. The fiber yarn volume fraction is varied by adjusting the yarn width. As can be seen from Figs. 7(a) and (b), both the in-plane shear stress–strain response and the stress relaxation behavior of the woven composite laminate exhibit a pronounced dependence on the fiber yarn volume fraction. Specifically, a higher fiber yarn volume fraction results in a larger shear stress at the same applied shear strain. This behavior can be attributed to the fact that the in-plane stiffness of the composite laminate is primarily governed by the amount of load-bearing fiber yarns.

5.3. Simulation of the column bending test

The Column Bending Test (CBT), developed by Fernandez and Murphey [70], was used to characterize the bending behavior of thin-ply high-strain composites, overcoming the limitations of traditional four-point bending tests, as shown in Fig. 8(a). In the CBT experiment set up, a pair of rigid clamps holds the thin-ply composite laminates, which is mounted on a materials testing machine. Under a compressive load, due to the special design, the gage section of the composite laminates is guided into a pure bending deformation state, which is the fundamental service condition for composite deployable structures. The reaction force and displacement measured by the testing machine can be used to derive the moment and curvature response of the composites during the test through simple and explicit geometric relations [70], enabling materials behavior characterization and constitutive model validation. Hamillage et al. [10] conducted loading–unloading CBT experiments of composite laminates under different maximum loading curvatures. The tested composites were plain-weave M30S/PMT-F7 laminates with a layup of $[45°]_3$, and the laminates' directions 1, 2, and n are shown in Figs. 8(b) and (c). The experiments lead to moment–curvature loading–unloading curves- and residual curvatures after unloading under different maximum loading curvatures. Under the same conditions, CBT experiments with loading-relaxation-unloading were also conducted on composite laminates with different maximum loading curvatures, providing moment–curvature loading-relaxation-unloading curves and residual curvatures after relaxation and unloading under different maximum loading curvatures.

A finite element model of the composite laminates CBT experiment was established using ABAQUS CAE, with geometry and boundary conditions consistent with the experimental investigation, as shown in Figs. 8(b) and (c). More detailed modeling settings can be found in recent works Long et al. [21],Yue et al. [52]. Key parameters of the finite element model include the laminate's width $\eta = 25.57$ mm, gauge length $s = 16.02$ mm, rigid clamp length $l = 25.4$ mm, and initial offset $D = 1.81$ mm. The composite laminate was discretized into 1519 fully integrated four-node shell elements (S4 in ABAQUS). The mesh independence of the finite element model was verified to ensure that the selected mesh density provides converged results. The mechanical behavior of the single-ply woven composite lamina was defined by a user-defined subroutine UMAT, which implements the viscoelastic–plastic constitutive model described in Section 3.3. The lamina material parameters were obtained from the two-step numerical homogenization developed in Section 4, as listed in Table A.5 in Appendix. The laminate behavior was defined using ABAQUS's built-in "composite layup" function based on classical laminate theory (CLT). This function calculates the stress and strain increments of each ply in the laminate during each time increment and integrates them through

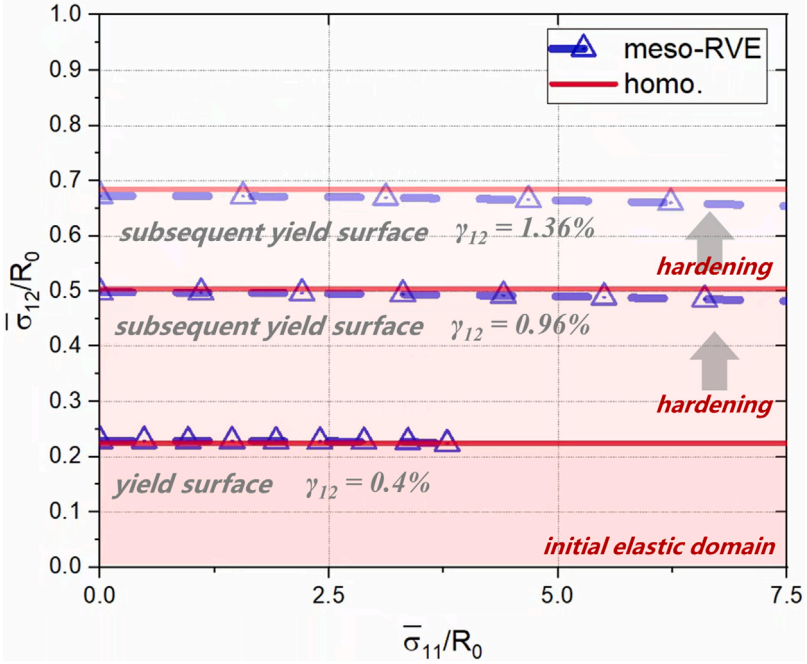

Fig. 6. Yield surface and subsequent yield surface evolution of the plain-weave meso-RVE model and the homogenized model in the $\sigma_{11} - \sigma_{12}$ plane.

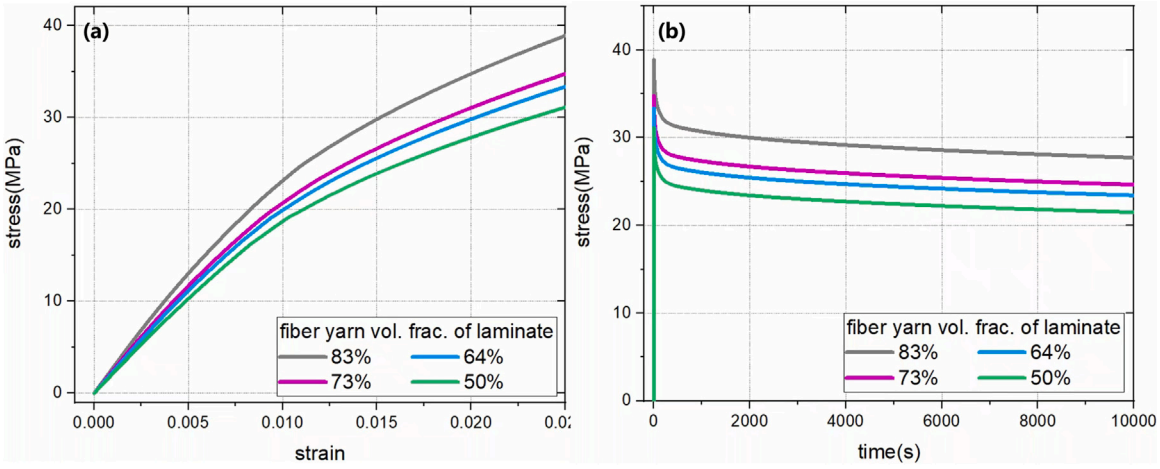

Fig. 7. Comparison of in-plane shear mechanical responses of laminates with different fiber yarn volume fractions: (**a**) stress–strain curves and (**b**) stress relaxation curves.

the thickness to obtain the nonlinear response of the shell elements. Finite element simulations of the composite laminate CBT experiments were conducted under two loading conditions: "loading-unloading" and "loading-relaxation-unloading", with a curvature loading rate of 0.1 mm^{-1}/min. It is worth noting that, due to unavoidable thickness deviations arising from specimen fabrication, as reported in the original literature [10], the tested specimens exhibit a maximum thickness of 0.209 mm, a minimum thickness of 0.194 mm, and an average thickness of 0.201 mm. Accordingly, finite element simulations of the CBT experiments were conducted by accounting for these three representative thickness values and were compared with the experimental results, as shown in Figs. 9 and 10.

Fig. 9 shows the moment per unit width-curvature curves of the composite laminate under different maximum loading curvatures captured by finite element simulations (red solid lines), with experimental observations also presented for comparison (blue dashed lines), demonstrating agreement between simulation and experiment. The slight deviations between simulation and experimental data observed are attributed to variations in the actual thickness of each sample due to the extremely thin composite laminates, while the finite element model used the average thickness reported across all experimental samples. It can be seen that the loading–unloading curves of the composite laminate do not overlap, exhibiting elastic hysteresis, which is a typical characteristic of viscoelastic materials, and the finite element simulation successfully captured this behavior.

Furthermore, the moment per unit width-curvature curves of the composite laminate under loading-relaxation-unloading conditions (orange solid lines) are shown in Fig. 10, with a relaxation time of 150 min. Experimental observation data are also presented for comparison (light blue dashed lines), showing consistency between simulation and experiment. The simulation successfully captured the moment relaxation of the composite laminate under constant curvature. Compared with the case without a relaxation process, the composites subjected to relaxation exhibited a more pronounced residual curvature after complete unloading. To illustrate this more clearly, a scatter plot of the maximum curvature during loading versus the residual curvature after unloading is shown in Fig. 11:

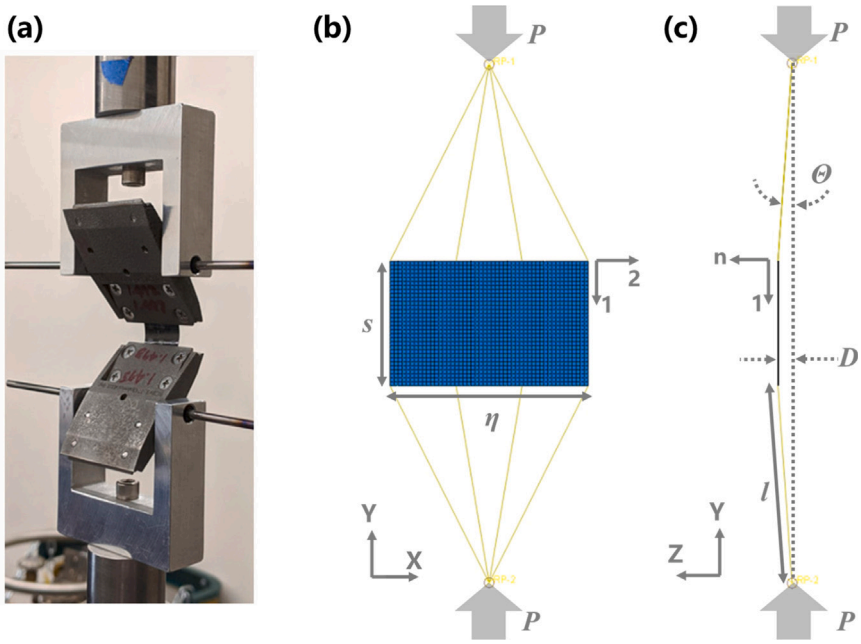

Fig. 8. Schematic of column bending test (CBT): (**a**) experimental setup (bending configuration, modified from Hamillage et al. [17]), (**b**) FE model in XY plane viewpoint, (**c**) FE model in YZ plane viewpoint.

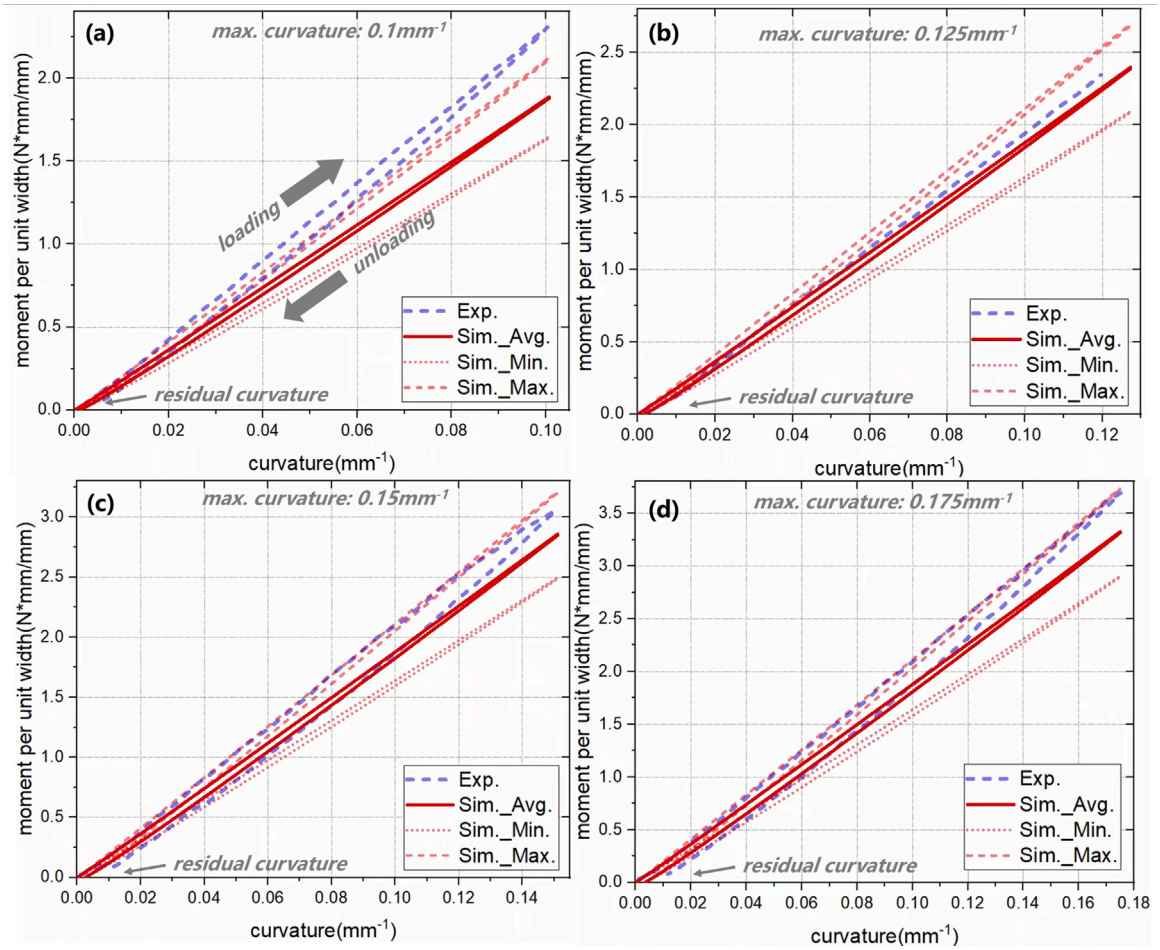

Fig. 9. Moment per unit length-curvature curves for different maximum curvatures under loading–unloading conditions, the experiments by Hamillage et al. [10] are shown for comparison, maximum curvature: (**a**) 0.1 mm^{-1}, (**b**) 0.125 mm^{-1}, (**c**) 0.15 mm^{-1}, (**a**) 0.175 mm^{-1}.

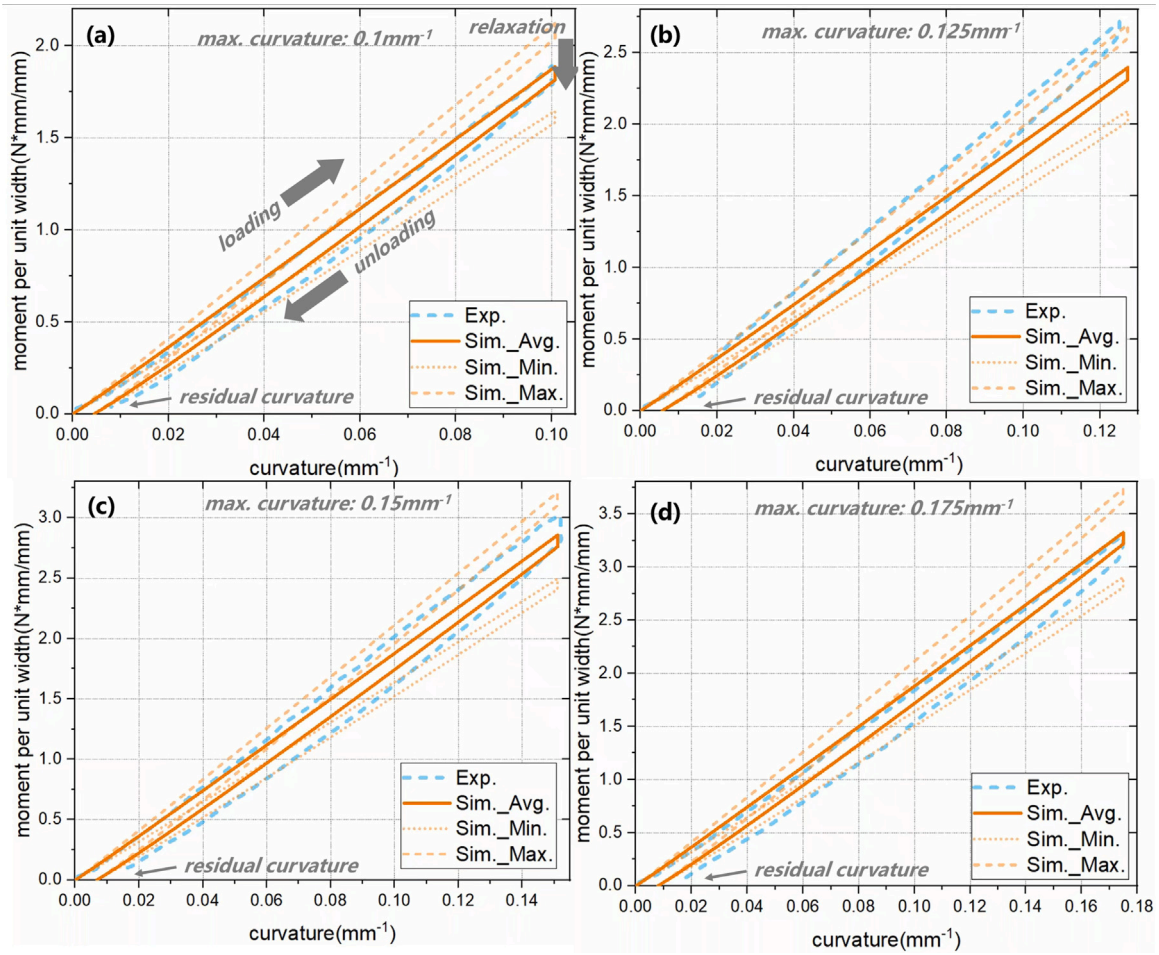

Fig. 10. Moment per unit length-curvature curves for different maximum curvatures under loading-relaxation-unloading conditions, the experiments by Hamillage et al. [10] are shown for comparison, maximum curvature: (**a**) 0.1 mm^{-1}, (**b**) 0.125 mm^{-1}, (**c**) 0.15 mm^{-1}, (**a**) 0.175 mm^{-1}.

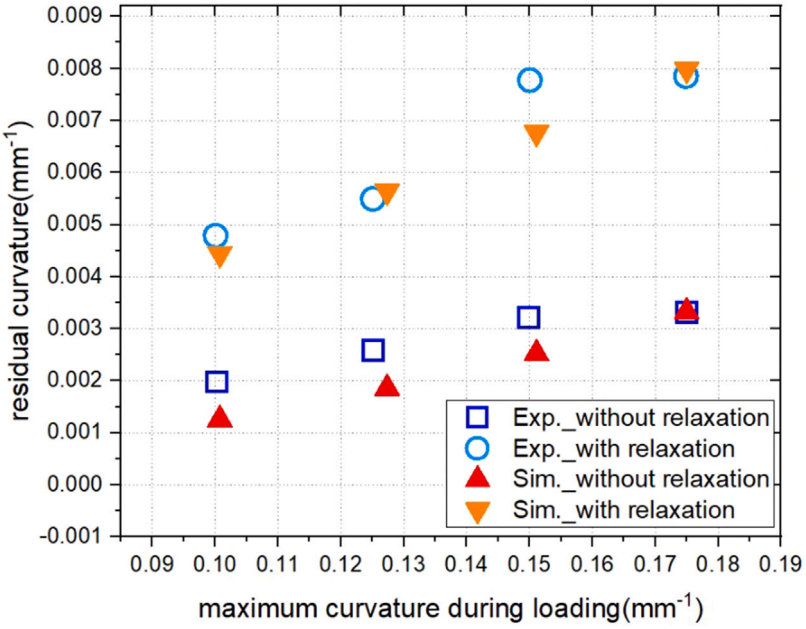

Fig. 11. Maximum curvature during loading vs. residual curvature, the experiments by Hamillage et al. [10] are shown for comparison.

The finite element simulation results in the above figure use the average laminate thickness. Two phenomena can be observed in Fig. 11: firstly, under the same testing conditions, the composite laminate exhibits greater residual curvature after complete unloading as the maximum curvature during loading increases. Secondly, compared to the composite laminates that did not undergo the relaxation process, those that experienced relaxation showed more pronounced residual curvature. It can be seen that the finite element simulation results successfully captured both phenomena and agreed with the experimental observations. The results presented in this section clearly demonstrate that the multiscale modeling scheme developed in this paper successfully identified the material parameters of the constitutive model and validated the effectiveness of the numerical homogenization procedure.

It should be noted that extending plasticity to viscoplasticity would allow the description of permanent deformation accumulation during the storage stage of composite deployable structures [10]. However, this extension introduces additional challenges in constitutive parameter calibration. Specifically, when viscous effects are simultaneously present in both the elastic and plastic responses, decoupling and identifying the corresponding parameters from experimental data become extremely difficult. In such cases, parameter identification must rely on optimization-based algorithms [32,59], which may result in calibrated parameters lacking clear physical interpretability. Therefore, the development of a physically consistent multiscale numerical homogenization-based parameter calibration framework for viscoelastic–viscoplastic constitutive models, capable of capturing the rate-dependent yielding behavior and time-dependent plastic strain accumulation observed in polymer matrix composites, should be regarded as an important direction for future research. In view of these challenges and for the sake of model simplicity, viscous effects in the plastic regime are not considered in the present paper. Nevertheless, the proposed framework has the potential to incorporate these effects in future developments. The constitutive model and material parameters established in this paper can be used for the design and analysis of composite deployable structures, and a preliminary example is presented in Section 6 to illustrate the application perspective in engineering design of the proposed approach.

6. Application to composite thin-walled lenticular tubes

Composite thin-walled lenticular tubes (CTLTs), made from thin-ply, high-strain composites, are widely used in deployable structures such as large solar sails and space solar array systems. A CTLT is a boom with a lenticular-shaped cross-section that, during service, is flattened and wound around a central hub to reduce stowage volume, as illustrated in the deployable structure shown in Fig. 1. Based on the present VE-P constitutive model for woven composites and the material parameters obtained through multiscale analysis, a finite element simulation was conducted to model the service periods of a 100 mm long mini-CTLT boom, including flattening, storage, deployment, and recovery periods. As shown in Fig. 12(a), the key geometric parameters of the mini-CTLT cross-section are: $R_1 = 26.5$ mm, $R_2 = 12$ mm, $w = 4.5$ mm, $H = 77$ mm, and $W = 86$ mm. These dimensions are based on the recent work of Hamillage et al. [69]. The mini-CTLT model is discretized with 6200 fully integrated four-node shell elements (S4 in ABAQUS). In the simulation, two rigid plates (defined as “discrete rigid” in ABAQUS), positioned above and below the mini-CTLT model, approach each other by 38 mm along the y-axis over 120 s to simulate the flattening process, as shown in Fig. 12(b). The flattened boom is then held in position for one year to simulate the storage periods during which stress relaxation occurs in the composites. Subsequently, the rigid plates are separated within 120 s, placing the mini-CTLT in a constraint-free state. Finally, the structure remains in this unrestrained state for 2×10^8 s (approximately 6.3 years) to simulate long-term recovery and permanent deformation.

Fig. 13(a) presents the deformation profiles and the distribution of the maximum in-plane principal stress in the mini-CTLT structure throughout the folding, storage, deployment, and recovery periods. It is observed that residual stresses remain in the structure after deployment, primarily attributed to the viscosity and plasticity responses of the composites. During the subsequent recovery period, wherein the structure is no longer subjected to external loads, the residual stress components induced by viscoelastic effects gradually dissipate, while those arising from irreversible plastic deformation persist. The evolution of the half cross-section shape of the mini-CTLT captured by the finite element simulation is shown in Fig. 13(b). Compared to the initial configuration (black solid line), the cross-section of the mini-CTLT after undergoing the flattening and storage periods exhibits pronounced residual deformation, characterized by a decrease in height and an increase in width. These geometric changes are detrimental to the load-bearing capacity of the CTLT and may adversely affect the interface compatibility between the CTLT and other subsystems in practical applications. After a recovery period of 30 days, the cross-sectional shape of the mini-CTLT gradually recovers toward its initial configuration. Similar trends have also been reported in the simulations by Hamillage et al. [69]. Fig. 13(c) presents the time-dependent recovery of the boom’s half cross-section height (red solid line). It can be observed that the height progressively approaches the initial value (black dotted line) as time increases. For comparison, the simulation results based on the viscoelastic (VE) constitutive model are also shown (blue dashed line). The VE model predicts that, over a sufficiently long recovery period, the residual deformation vanishes entirely. In contrast, the current VE-P model successfully captures the irreversible deformation of the mini-CTLT structure, thereby expanding the modeling capabilities of VE model-based methods. This section provides a representative example of the mechanical behavior analysis of a mini-CTLT structure. The proposed modeling and analysis framework is general and can be further extended to more complex and practically relevant configurations. These include full-scale CTLT structures as well as larger and more intricate deployable systems, such as solar array support booms, for the investigation of their mechanical behavior under service conditions.

7. Conclusions

The present paper develops a multiscale modeling framework for high-strain composites. Three viscoelastic–plastic (VE-P) constitutive models are formulated to characterize the mechanical behaviors of the polymer matrix, fiber yarns, and single-ply woven composite lamina, respectively. Based on the known mechanical properties of the polymer matrix and fibers, a two-step numerical homogenization procedure is proposed to identify the material parameters of the woven composite lamina. These parameters are subsequently used in time-dependent mechanical simulations of deployable structures constructed from woven composite laminates. Finite element simulations are conducted for two column bending test (CBT) loading scenarios: loading-unloading and loading-relaxation-unloading of woven composite laminates. The simulation results show good agreement with experimental observations, thereby validating both the proposed constitutive models and the numerical homogenization strategy.

The contributions of this work are threefold. First, although our recent study [52] proposed a viscoelastic-viscoplastic (VE-VP) constitutive model for composites, calibrating the model requires extensive and costly experimental data. While the numerical homogenization method developed by Liu et al. [51] addressed the parameter identification problem for transverse behavior in unidirectional composites, it is essentially limited to calibrating isotropic nonlinear constitutive models. In contrast, the present paper develops a two-step numerical homogenization strategy tailored to identify the material parameters of a composite VE-P model, providing a complete and generalizable solution. Second, using the proposed constitutive model and the material

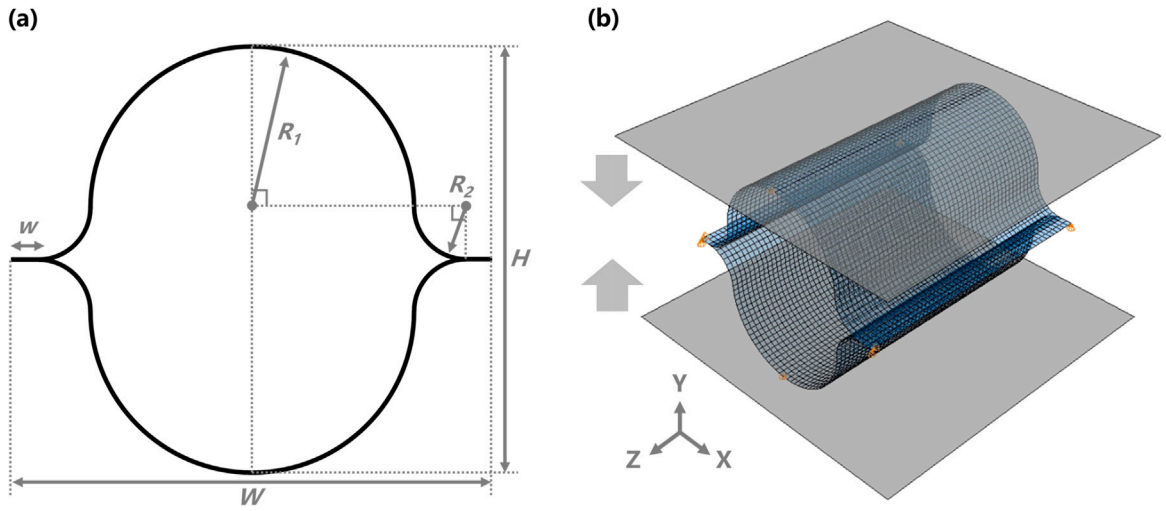

Fig. 12. Mini composite thin-walled lenticular tube (mini-CTLT) model: (**a**) cross-section geometry, (**b**) finite element model.

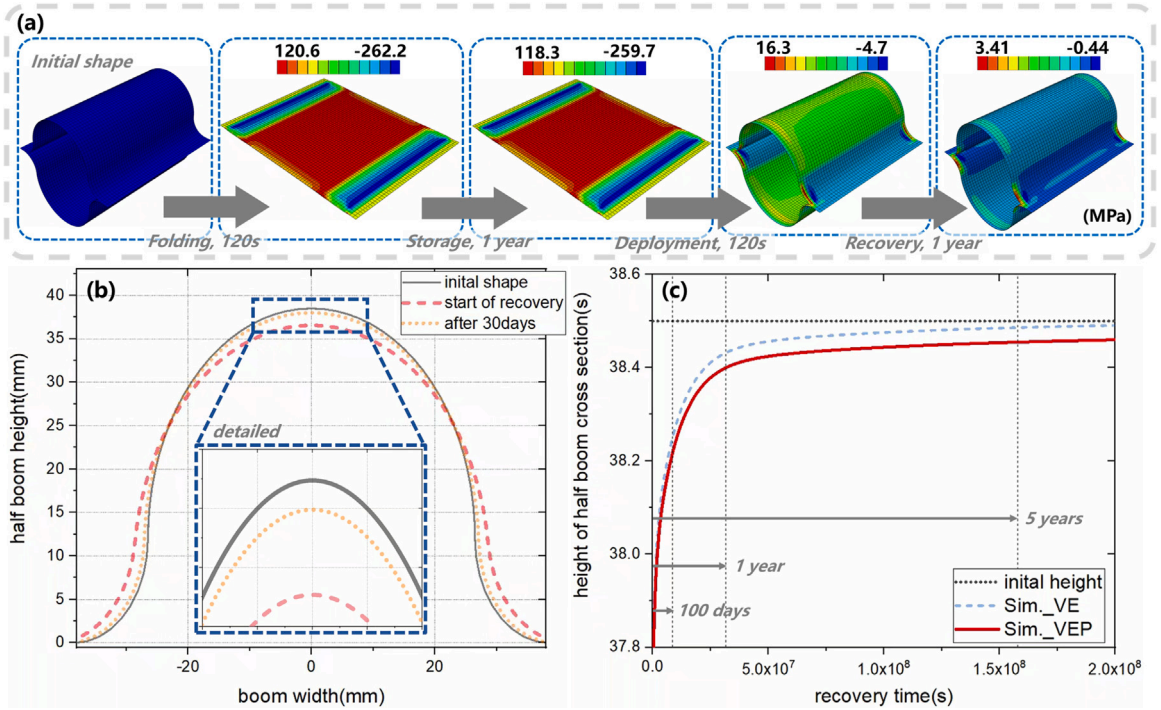

Fig. 13. Simulated results of miniCTLT: (**a**) Deformation and maximum in-plane principal stress distribution during folding, storage, deployment, and recovery periods, (**b**) the top half cross-section shape of the tube at different instances of recovery, (**c**) the height history of the tube cross-section during the recovery period.

parameters obtained via numerical homogenization, we conduct finite element simulations of CBT experiments under different loading conditions. The simulations successfully capture the time-dependent mechanical response of composite laminates and resolve the overestimation issue observed in previous CBT simulations based on viscoelastic shell models, such as those reported by Hamillage et al. [17]. Finally, the developed constitutive model and obtained parameters are applied to simulate the service periods of a mini composite thin-walled lenticular tube (mini-CTLT) boom, including flattening, storage, deployment, and recovery periods. The simulation captures typically time-dependent behaviors of deployable structures, such as shape recovery and permanent deformation, demonstrating the application perspective of the proposed multiscale modeling framework in the design and performance prediction of composite deployable structures.

The present paper also has several limitations that warrant further investigation in future work. First, the proposed model tends to overestimate the plastic strain of the polymer matrix after long-term recovery. Introducing a nonlinear viscoelastic–plastic constitutive formulation may enable more accurate predictions of the long-term recovery behavior. Second, the two-scale numerical homogenization approach developed in this paper is based on a viscoelastic–plastic constitutive description of composite materials. To further extend the applicability of the framework, it is necessary to develop effective parameter identification strategies for viscoelastic–viscoplastic constitutive models of composites, enabling the decoupled calibration of viscous parameters associated with the elastic and plastic responses from experimental or virtual experimental data. Such advancements would ultimately allow for the prediction and analysis of permanent

residual deformation accumulation during the storage stage of composite deployable structures. Nevertheless, the multiscale analysis and parameter identification framework established in this paper has been systematically validated and successfully addresses the fundamental modeling and calibration challenges at the framework level. As such, it provides a well-founded basis for future extensions toward these more advanced and challenging modeling directions.

CRediT authorship contribution statement

Xiaowei Yue: Writing – original draft, Visualization, Validation, Software, Methodology, Investigation, Funding acquisition, Formal analysis, Data curation, Conceptualization. **Ruiwen Guo:** Visualization, Validation, Software, Formal analysis. **Ning An:** Writing – review & editing, Writing – original draft, Validation, Supervision, Resources, Project administration, Investigation. **Hao Jin:** Validation, Software, Formal analysis. **Jinxiong Zhou:** Writing – review & editing, Supervision, Resources, Project administration, Funding acquisition, Conceptualization.

Declaration of competing interest

The authors declare that they have no known competing financial interests or personal relationships that could have appeared to influence the work reported in this paper.

Acknowledgments

This research is supported by the National Natural Science Foundation of China (grant 11972277 and 12202295), and the International (Regional) Cooperation and Exchange Projects of the National Natural Science Foundation of China (grant W2421002), and by the Fundamental Research Funds for the Central Universities, China (grant xzy022024052), and by Sichuan Science and Technology Program, China (grant 2025ZNSFSC0845).

Appendix. Materials parameters and calibration procedure

The material parameters calibration process for the three constitutive models includes the PMT-F7 polymer matrix, the unidirectional M30S/PMT-F7 fiber yarn, and the M30S/PMT-F7 woven composite lamina.

I. Calibration of the polymer matrix: The calibration of the isotropic viscoelastic–plastic constitutive model for the PMT-F7 polymer matrix (see Section 3.1) is divided into the viscoelastic and plastic components. The viscoelastic relaxation moduli for PMT-F7 are referenced from the work of Hamillage et al. [69], as shown in Table A.2. The calibration of the present constitutive model requires obtaining the values of the components in the Prony series expression for the shear and volumetric relaxation moduli, as in Eqs. (6) and (7). This paper assumes that the shear and volumetric relaxation times are equal, with the Poisson's ratio $\nu = 0.3$ held constant. The shear and volumetric relaxation moduli are calculated as follows:

$$G(t) = \frac{E(t)}{2(1+\nu)} \tag{A.1}$$

$$K(t) = \frac{E(t)}{3(1-2\nu)} \tag{A.2}$$

The material parameters for the plastic part of PMT-F7 are calibrated using the experimental observation data from Hamillage et al. [10]. In this paper, the J2 yield criterion is used to describe the yield and plastic flow behavior of the PMT-F7 polymer. The experimental stress–strain data are converted into equivalent stress σ_{eq} vs. equivalent plastic strain p data through Eqs. (A.3), (A.4) and (A.5):

$$\sigma_{eq} = \sigma \tag{A.3}$$

$$\varepsilon^p = \varepsilon - \frac{\sigma}{E_0} \tag{A.4}$$

$$p = \varepsilon^p \tag{A.5}$$

where E_0 denotes the initial modulus of the PMT-F7 polymer. The processed experimental data are shown as black triangular dots in Fig. A.1, and are fitted using the hardening function of the PMT-F7 polymer (red solid line). The calibrated material parameters for the PMT-F7 polymer are summarized in Table A.3.

II. Calculation of the unidirectional M30S/PMT-F7 fiber yarn: The calibration of the viscoelastic–plastic constitutive model for the M30S/PMT-F7 fiber yarn (see Section 3.2) is divided into viscoelastic and plastic components. The mechanical response data in terms of macroscopic stress $\bar{\sigma}$ and macroscopic strain $\bar{\varepsilon}$ used for model calibration are obtained from virtual testing on a micro-RVE model of the unidirectional fiber yarn (micro-RVE in Fig. 2(a)). The macroscopic stress $\bar{\sigma}$ and macroscopic strain $\bar{\varepsilon}$ are computed by Eqs. (A.6) and (A.7):

$$\bar{\sigma} = \boldsymbol{P}^{rs}/A^{rs} \tag{A.6}$$

$$\bar{\varepsilon} = \boldsymbol{E}^{ap}/L^{ap} \tag{A.7}$$

where $\boldsymbol{E}^{ap}$ denotes the imposed displacement applied to the reference points to which one set of opposite faces of the micro-RVE is constrained, and L^{ap} represents the micro-RVE length perpendicular to the loading surface. $\boldsymbol{P}^{rs}$ denotes the reaction force at the reference points on the constrained face, and A^{rs} is the area of the responding surface. By applying a constant macroscopic strain $\bar{\varepsilon}^{cst}$ to the micro-RVE along various directions, the corresponding macroscopic stress history $\bar{\sigma}(t)$ can be obtained:

$$\begin{pmatrix} \bar{\sigma}_{11}(t) \\ \bar{\sigma}_{22}(t) \\ \bar{\sigma}_{33}(t) \\ \bar{\sigma}_{23}(t) \\ \bar{\sigma}_{13}(t) \\ \bar{\sigma}_{12}(t) \end{pmatrix} = \begin{pmatrix} C_{11}^{UD}(t) & C_{12}^{UD}(t) & C_{13}^{UD}(t) & 0 & 0 & 0 \\ C_{12}^{UD}(t) & C_{22}^{UD}(t) & C_{23}^{UD}(t) & 0 & 0 & 0 \\ C_{13}^{UD}(t) & C_{23}^{UD}(t) & C_{22}^{UD}(t) & 0 & 0 & 0 \\ 0 & 0 & 0 & C_{44}^{UD}(t) & 0 & 0 \\ 0 & 0 & 0 & 0 & C_{55}^{UD}(t) & 0 \\ 0 & 0 & 0 & 0 & 0 & C_{55}^{UD}(t) \end{pmatrix} \begin{pmatrix} \bar{\varepsilon}_{11}^{cst} \\ \bar{\varepsilon}_{22}^{cst} \\ \bar{\varepsilon}_{33}^{cst} \\ \bar{\gamma}_{23}^{cst} \\ \bar{\gamma}_{13}^{cst} \\ \bar{\gamma}_{12}^{cst} \end{pmatrix} \tag{A.8}$$

The fiber yarn is assumed to exhibit transverse isotropy. Based on Eq. (A.8), the time evolution of the components of the relaxation tensor can be computed. Specifically, by applying a time-invariant macroscopic strain $\bar{\varepsilon}^{cst} = (\bar{\varepsilon}_{11}^{cst}, 0, 0, 0, 0, 0)^T$ to the micro-RVE, the resulting macroscopic stress response is given by $\bar{\sigma}(t) = (\bar{\sigma}_{11}(t), \bar{\sigma}_{22}(t), \bar{\sigma}_{33}(t), 0, 0, 0)^T$. This allows the calculation of the relaxation tensor components as $C_{11}^{UD}(t) = \bar{\sigma}_{11}(t)/\bar{\varepsilon}_{11}^{cst}$, $C_{12}^{UD}(t) = \bar{\sigma}_{22}(t)/\bar{\varepsilon}_{11}^{cst}$, and $C_{13}^{UD}(t) = \bar{\sigma}_{33}(t)/\bar{\varepsilon}_{11}^{cst}$. The time-dependent responses of the remaining components of the relaxation tensor can be determined in a similar manner, as shown by the black square dots in Fig. A.2. Each component of the relaxation tensor is fitted using a Prony series (Eq. (16)), as illustrated by the red solid lines, to calibrate the viscoelastic parameters of the fiber yarn constitutive model.

The macroscopic strain is applied to the transverse and shear directions of the micro-RVE in a ramp-loading manner, and the corresponding macroscopic stress responses are computed. Based on the expression for the equivalent stress of the fiber yarn (Eq. (24)), the relationships between the stress components in the transverse and shear directions and the equivalent stress can be established as follows:

$$\sigma_{eq} = \bar{\sigma}\sqrt{\frac{3}{2}}a = h(a)\bar{\sigma} \tag{A.9}$$

The anisotropy coefficient a depends on the direction of the macroscopic stress. Specifically, $a = 1$ when the macroscopic stress $\bar{\sigma}$ corresponds to $\bar{\sigma}_{22}$ or $\bar{\sigma}_{33}$; $a = a_{44}$ for $\bar{\sigma}_{23}$; and $a = a_{66}$ for $\bar{\sigma}_{12}$ or $\bar{\sigma}_{13}$. The calculation of the plastic strain follows the same procedure as described

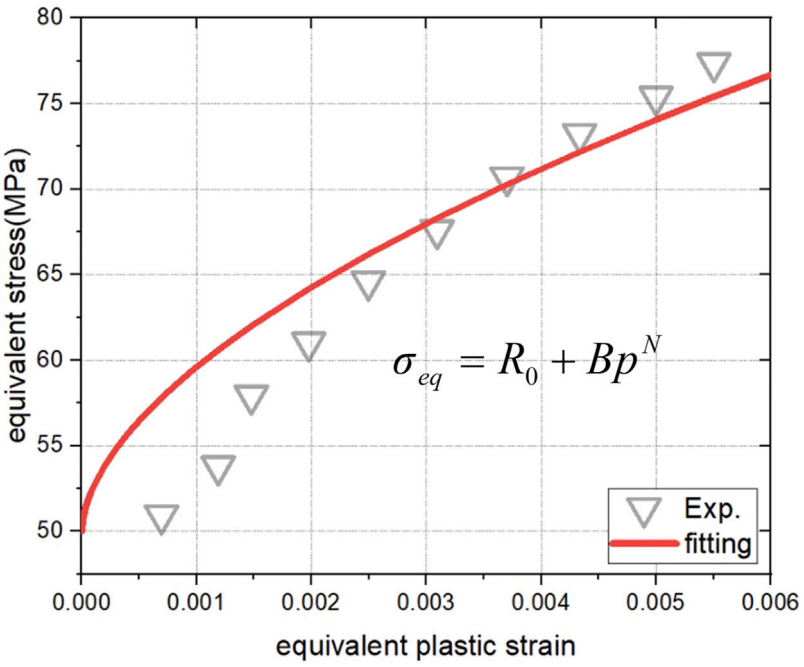

Fig. A.1. Fitting equivalent stress-equivalent plastic strain experimental data of FMT-F7 polymer based on the hardening function.

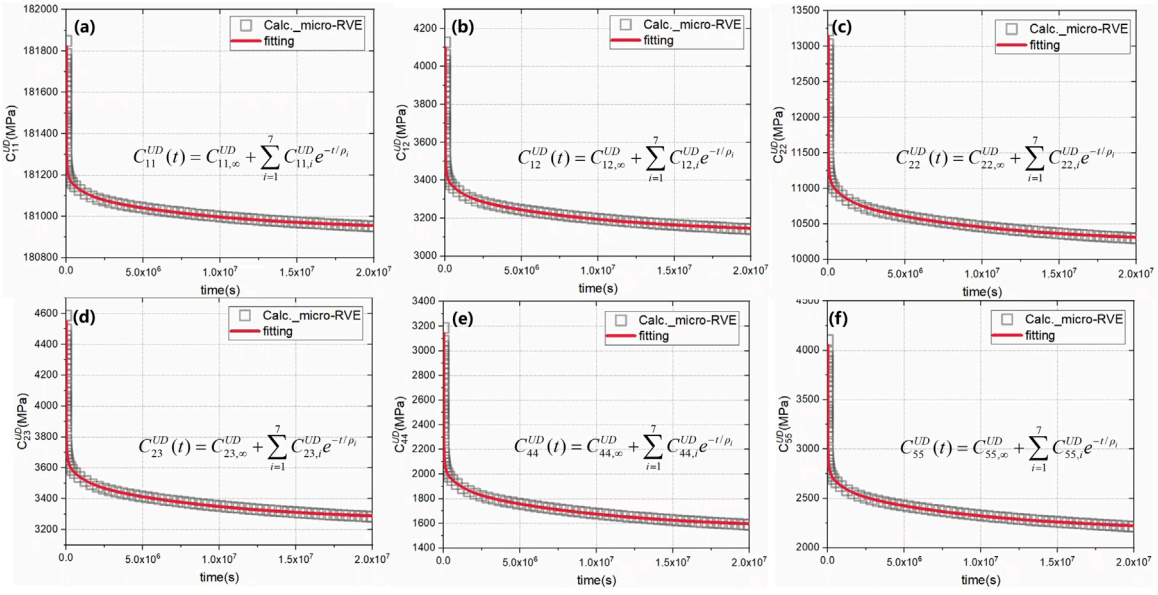

Fig. A.2. Fitting relaxation data calculated by unidirectional micro-RVE based on the Prony's series for fiber yarn: (**a**) C_{11}^{UD}, (**b**) C_{12}^{UD}, (**c**) C_{22}^{UD}, (**d**) C_{23}^{UD}, (**e**) C_{44}^{UD}, (**f**) C_{55}^{UD}.

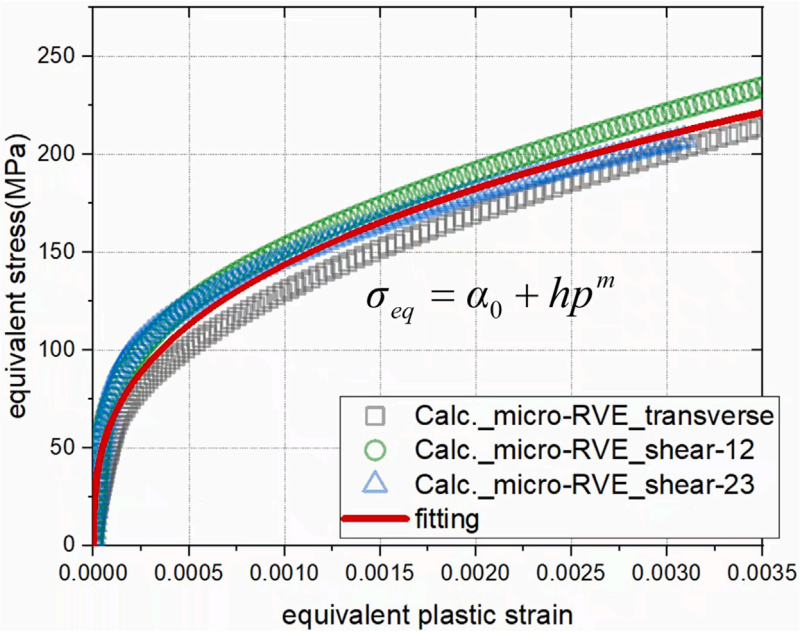

Fig. A.3. Fitting equivalent stress-equivalent plastic strain data calculated by unidirectional micro-RVE based on the hardening function for fiber yarn.

above (see Eq. (A.4)). The corresponding equivalent plastic strain p is given by:

$$p = \frac{\varepsilon^p}{h(a)} \tag{A.10}$$

Through iterative calibration, the anisotropy coefficients were determined as $a_{44} = 4$ and $a_{55} = 3$. The resulting master curve of equivalent stress versus equivalent plastic strain is shown as scattered dots in Fig. A.3. The data were fitted using the hardening function of the fiber yarn (red solid line). The calibrated material parameters for the unidirectional M30S/PMT-F7 fiber yarn are summarized in Table A.4.

III. Calculation of the woven M30S/PMT-F7 composite lamina: The calibration of the viscoelastic–plastic constitutive model for the M30S/PMT-F7 woven composite lamina (see Section 3.3) is divided into viscoelastic and plastic components. The mechanical response data in terms of macroscopic stress $\bar{\sigma}$ and macroscopic strain $\bar{\varepsilon}$ used for model calibration are obtained from virtual testing on a plain-weave meso-RVE model (meso-RVE in Fig. 2(b)). The calculation method is the same as that for micro-RVE, as detailed in Eqs. (A.6) and (A.7). By applying constant macroscopic strain $\bar{\varepsilon}^{cst}$ in different directions on the meso-RVE, the corresponding macroscopic stress history $\bar{\sigma}(t)$ can be obtained:

$$\begin{pmatrix} \bar{\sigma}_{11}(t) \\ \bar{\sigma}_{22}(t) \\ \bar{\sigma}_{12}(t) \end{pmatrix} = \begin{pmatrix} C_{11}^{PW}(t) & C_{12}^{PW}(t) & 0 \\ C_{12}^{PW}(t) & C_{11}^{PW}(t) & 0 \\ 0 & 0 & C_{33}^{PW}(t) \end{pmatrix} \begin{pmatrix} \varepsilon_{11}^{cst} \\ \varepsilon_{22}^{cst} \\ \gamma_{12}^{cst} \end{pmatrix} \tag{A.11}$$

Similar to the fiber yarn, the time evolution in the components of the relaxation tensor can be calculated using Eq. (A.11), as shown by the black square dots in Figs. A.4(a), (b), and (c). The components of the relaxation tensor are fitted using a Prony series (Eq. (16) in plane stress form), and the red solid lines represent the fitted curves. This process allows for the determination of the material parameters of the viscoelastic part of the constitutive model for woven composite lamina.

Shear strains are applied in a ramp manner to the meso-RVE, and the corresponding macroscopic stress response is calculated. Based on the equivalent stress expression for the woven composite lamina (Eq. (31)), the relationship between the stress and the equivalent stress in the shear direction can be obtained as follows:

$$\sigma_{eq} = \bar{\sigma}\sqrt{3} \tag{A.12}$$

Table A.1
Material Properties of M30S fiber [17].

Properties	Values, Unit
E_1	294000, MPa
E_2	29148, MPa
G_{12}	11310, MPa
G_{23}	10000, MPa
$\nu_{12} = \nu_{13}$	0.2
ν_{23}	0.46

Table A.2
Prony coefficients for PMT-F7 epoxy matrix [69].

i	ρ_i (s)	E_i (N/mm^2)
∞	–	2535.2
1	0.96	168.6
2	9.7	111.6
3	93.78	221.7
4	981.1	63.1
5	9283	235.5
6	97 210	84.8
7	963 100	109.5
8	9 472 000	151.6
9	56 310 000	164.4

The calculation method for plastic strain is the same as described above, as shown in Eq. (A.4). The corresponding equivalent plastic strain p is given by:

$$p = \frac{\varepsilon^p}{\sqrt{3}} \tag{A.13}$$

The resulting equivalent stress-equivalent plastic strain relationship is shown as scatter dots in Fig. A.4(d). The experimental data are fitted using the hardening function of the woven composite lamina (red solid line). The calibrated material parameters for the woven M30S/PMT-F7 composite lamina are presented in Table A.5.

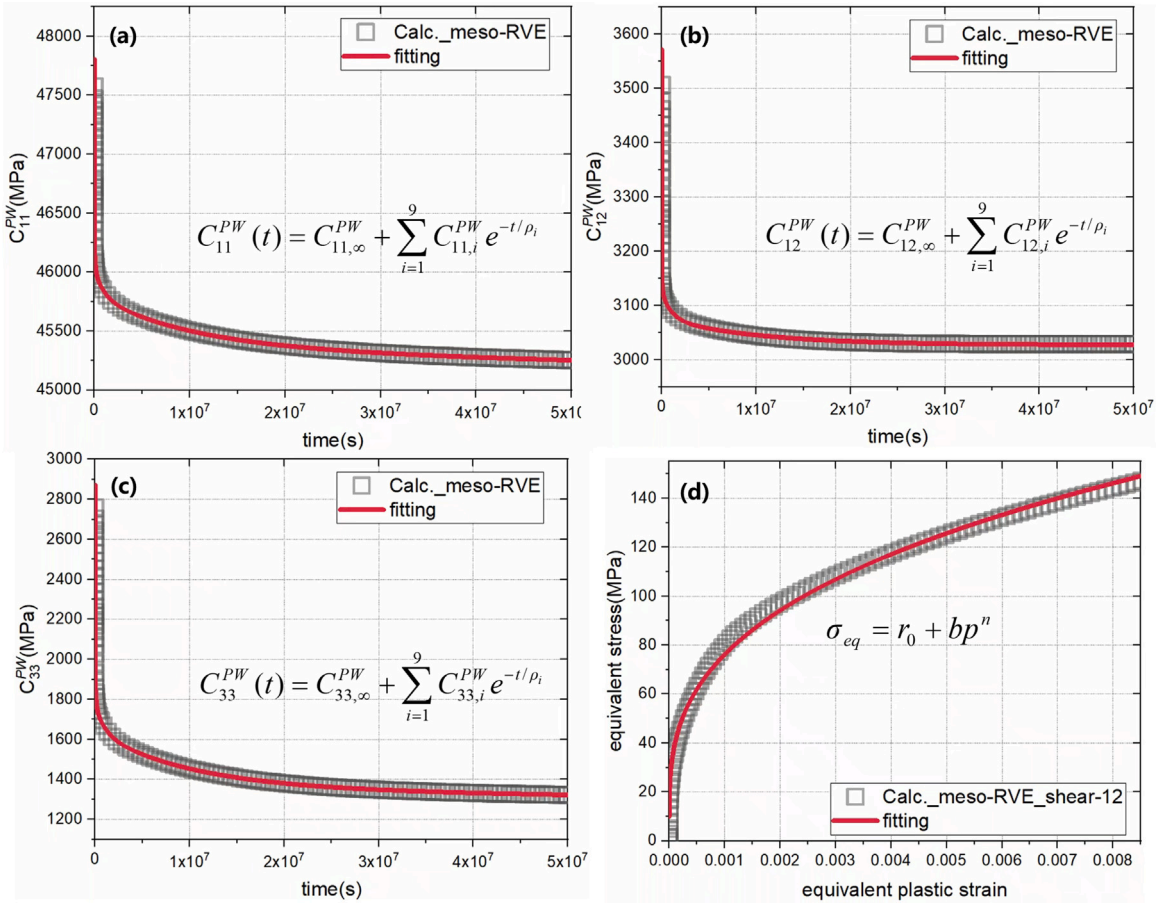

Fig. A.4. Woven lamina constitutive model parameter fitting, fitting relaxation data calculated by plain-weave meso-RVE based on the Prony's series for fabric lamina: (**a**) C_{11}^{PW}, (**b**) C_{12}^{PW}, (**c**) C_{33}^{PW}, and (**d**) fitting equivalent stress-equivalent plastic strain data calculated by plain-weave meso-RVE based on the hardening function for fabric lamina.

Table A.3
VE-P model parameters for PMT-F7 epoxy matrix.

viscoelastic					reference
i	g_i (s)	G_i (MPa)	k_i (s)	K_i (MPa)	
∞	–	975.08	–	2112.67	Hamillage et al. [69]
1	0.96	64.85	0.96	140.5	Hamillage et al. [69]
2	9.7	42.92	9.7	93	Hamillage et al. [69]
3	93.78	85.27	93.78	184.75	Hamillage et al. [69]
4	981.1	24.27	981.1	52.58	Hamillage et al. [69]
5	9283	90.58	9283	196.25	Hamillage et al. [69]
6	97 210	32.62	97 210	70.67	Hamillage et al. [69]
7	963 100	42.12	963 100	91.25	Hamillage et al. [69]
8	9 472 000	58.31	9 472 000	126.33	Hamillage et al. [69]
9	56 310 000	63.23	56 310 000	137	Hamillage et al. [69]
plastic					
hardening laws:	B = 495 MPa		N = 0.57		fit [10]
	R_0 = 50 MPa				fit [10]

Table A.4
VE-P model parameters for unidirectional M30S/PMT-F7 fiber yarn.

viscoelastic								reference
i	ρ_i (s)	$C^{UD}_{11,i}$ (MPa)	$C^{UD}_{12,i}$ (MPa)	$C^{UD}_{22,i}$ (MPa)	$C^{UD}_{23,i}$ (MPa)	$C^{UD}_{44,i}$ (MPa)	$C^{UD}_{55,i}$ (MPa)	
∞	–	180 931	3118.723	10 226.59	3252.65	1550.36	2166.39	calculated
1	10	159.175	168.6387	493.546	229.145	266.86	299.166	calculated
2	100	150.613	163.597	483.332	218.854	263.698	306.046	calculated
3	1000	62.647	68.6387	201.168	91.091	109.525	126.893	calculated
4	1×10^4	186.757	205.522	611.288	271.78	333.36	394.793	calculated
5	1×10^5	72.06	81.58	245.289	105.77	135.066	166.107	calculated
6	1×10^6	79.908	88.234	263.821	115.65	142.9	171.055	calculated
7	1×10^7	180.256	204.811	618.812	263.19	340.58	424.716	calculated
plastic								
hardening laws:		h = 1570.14 MPa		m = 0.346				calculated
		α_0 = 10 MPa						calculated
anisotropy coefficient:		a_{44} = 4		a_{66} = 3				calculated

Table A.5
VE-P model parameters for woven M30S/PMT-F7 composite lamina.

viscoelastic						reference
i	ρ_i (s)	$C^{PW}_{11,i}$ (MPa)	$C^{PW}_{12,i}$ (MPa)	$C^{PW}_{22,i}$ (MPa)	$C^{PW}_{66,i}$ (MPa)	
∞	–	45 051.19	3027.051	45 051.19	1255.95	calculated
1	1	316.271	87.83	316.271	145.325	calculated
2	10	284.993	89.94	284.993	203.618	calculated
3	100	397.642	103.679	397.642	250.067	calculated
4	1000	135.188	35.126	135.188	90.191	calculated
5	1×10^4	470.014	106.146	470.014	297.689	calculated
6	1×10^5	182.112	25.93	182.112	115.365	calculated
7	1×10^6	219.656	46.4	219.656	132.806	calculated
8	1×10^7	420.37	49.78	420.37	275.037	calculated
9	1×10^8	328.39	2.07×10^{-13}	328.39	106.681	calculated
plastic						
hardening laws:	b = 726.2 MPa		n = 0.3467			calculated
	r_0 = 10 MPa					calculated

Data availability

The raw/processed data required to reproduce these findings are available to download from https://github.com/XJTU-Zhou-group/ABAQUS_UMAT_HSCmultiscaleVEP.

References

[1] Ma X, An N, Cong Q, Bai J-B, Wu M, Xu Y, Zhou J, Zhang D, Zhang T, Guo R, et al. Design, modeling, and manufacturing of high strain composites for space deployable structures. Commun Eng 2024;3(1):78.

[2] Khare V, Yapa Hamillage MM, Raghu R, Mashin A, Kwok K, Ferraro S. Shape accuracy analysis of starshade petals. In: AIAA SCITECH 2025 forum. 2025, p. 1195.

[3] Liu T-W, Bai J-B, Fantuzzi N, Zhang X. Thin-walled deployable composite structures: a review. Prog Aerosp Sci 2024;146:100985.

[4] Murphey TW, Francis W, Davis B, Mejia-Ariza JM. High strain composites. In: 2nd AIAA spacecraft structures conference. 2015, p. 0942.

[5] Kwok K, Pellegrino S. Folding, stowage, and deployment of viscoelastic tape springs. AIAA J 2013;51(8):1908–18.

[6] Kwok K, Pellegrino S. Micromechanics models for viscoelastic plain-weave composite tape springs. AIAA J 2017;55(1):309–21.

[7] Guo R, Jin X, Jia Q, Ma X, An N, Zhou J. Folding, stowage, and deployment of composite thin-walled lenticular tubes. Acta Astronaut 2023;213:567–77.

[8] Jinfeng D, Ning A, Qilong J, Xiaofei M. Deployment analysis of composite thin-walled lenticular tubes with effect of storage time and temperature. Chin J Aeronaut 2024;37(1):162–72.

[9] Salazar JE, Fernandez JM. Experimental characterization of the dimensional stability of deployable composite booms during stowage. In: AIAA sciTech 2021 forum. 2021, p. 0195.

[10] Hamillage MY, Klimm W, Kwok K. Permanent shape change of thin-ply composites. In: AIAA scitech 2022 forum. 2022, p. 1117.

[11] Shirinbayan M, Fitoussi J, Bocquet M, Meraghni F, Surowiec B, Tcharkhtchi A. Multi-scale experimental investigation of the viscous nature of damage in advanced sheet molding compound (A-SMC) submitted to high strain rates. Compos Part B: Eng 2017;115:3–13.

[12] Jäger J, Sause MG, Burkert F, Moosburger-Will J, Greisel M, Horn S. Influence of plastic deformation on single-fiber push-out tests of carbon fiber reinforced epoxy resin. Compos Part A: Appl Sci Manuf 2015;71:157–67.

[13] Courtois A, Marcin L, Benavente M, Ruiz E, Lévesque M. Numerical multi-scale homogenization approach for linearly viscoelastic 3D interlock woven composites. Int J Solids Struct 2019;163:61–74.

[14] Kueh A, Pellegrino S. ABD matrix of single-ply triaxial weave fabric composites. In: 48th AIAA/aSME/ASCE/AHS/aSC structures, structural dynamics, and materials conference. 2007, p. 2161.

[15] Mallikarachchi H. Predicting mechanical properties of thin woven carbon fiber reinforced laminates. Thin-Walled Struct 2019;135:297–305.

[16] Jin H, An N, Jia Q, Ma X, Zhou J. A mesoscale computational approach to predict ABD matrix of thin woven composites. Compos Struct 2024;337:118031.

[17] Hamillage MY, Leung C, Kwok K. Viscoelastic modeling and characterization of thin-ply composite laminates. Compos Struct 2022;280:114901.

[18] Yu W. Simplified formulation of mechanics of structure genome. AIAA J 2019;57(10):4201–9.

[19] Rouf K, Liu X, Yu W. Multiscale structural analysis of textile composites using mechanics of structure genome. Int J Solids Struct 2018;136:89–102.

[20] Liu X, Rouf K, Peng B, Yu W. Two-step homogenization of textile composites using mechanics of structure genome. Compos Struct 2017;171:252–62.

[21] Long Y, Rique O, Fernandez JM, Bergan AC, Salazar JE, Yu W. Simulation of the column bending test using an anisotropic viscoelastic shell model. Compos Struct 2022;288:115376.

[22] Liu X, Tang T, Yu W, Pipes RB. Multiscale modeling of viscoelastic behaviors of textile composites. Internat J Engrg Sci 2018;130:175–86.

[23] Brinkmeyer A, Pellegrino S, Weaver PM. Effects of long-term stowage on the deployment of bistable tape springs. J Appl Mech 2016;83(1):011008.

[24] Mao H, Shipsha A, Tibert G. Design and analysis of laminates for self-deployment of viscoelastic bistable tape springs after long-term stowage. J Appl Mech 2017;84(7):071004.

[25] Borowski EC, Soliman EM, Khan AI, Taha MMR. Stowage and deployment of a viscoelastic orthotropic carbon-fiber composite tape spring. J Spacecr Rockets 2018;55(4):829–40.

[26] Fernandes P, Sousa B, Marques R, Tavares JMR, Marques A, Jorge RN, Pinto R, Correia N. Influence of relaxation on the deployment behaviour of a CFRP composite elastic-hinge. Compos Struct 2021;259:113217.

[27] An N, Jia Q, Jin H, Ma X, Zhou J. Multiscale modeling of viscoelastic behavior of unidirectional composite laminates and deployable structures. Mater Des 2022;219:110754.

[28] Kunakorn-ong P, Santer M. Optimal design of tube flexure cut-out geometries for viscoelastic resilience and deployment performance. Acta Astronaut 2024;216:282–94.
[29] Klimm W, Kwok K. Surface accuracy of viscoelastic composite thin-shell deployable reflector antennas. In: AIAA scitech 2020 forum. 2020, p. 0932.
[30] Hill R. Continuum micro-mechanics of elastoplastic polycrystals. J Mech Phys Solids 1965;13(2):89–101.
[31] Molinari A, Canova G, Ahzi S. A self consistent approach of the large deformation polycrystal viscoplasticity. Acta Metall 1987;35(12):2983–94.
[32] Miled B, Doghri I, Brassart L, Delannay L. Micromechanical modeling of coupled viscoelastic–viscoplastic composites based on an incrementally affine formulation. Int J Solids Struct 2013;50(10):1755–69.
[33] Doghri I, Adam L, Bilger N. Mean-field homogenization of elasto-viscoplastic composites based on a general incrementally affine linearization method. Int J Plast 2010;26(2):219–38.
[34] Pierard O, LLorca J, Segurado J, Doghri I. Micromechanics of particle-reinforced elasto-viscoplastic composites: finite element simulations versus affine homogenization. Int J Plast 2007;23(6):1041–60.
[35] Pierard O, Doghri I. An enhanced affine formulation and the corresponding numerical algorithms for the mean-field homogenization of elasto-viscoplastic composites. Int J Plast 2006;22(1):131–57.
[36] Kouznetsova V, Brekelmans W, Baaijens F. An approach to micro-macro modeling of heterogeneous materials. Comput Mech 2001;27(1):37–48.
[37] Ghosh S, Lee K, Moorthy S. Multiple scale analysis of heterogeneous elastic structures using homogenization theory and Voronoi cell finite element method. Int J Solids Struct 1995;32(1):27–62.
[38] Feyel F, Chaboche J-L. FE2 multiscale approach for modelling the elastoviscoplastic behaviour of long fibre SiC/Ti composite materials. Comput Methods Appl Mech Engrg 2000;183(3–4):309–30.
[39] Coenen E, Kouznetsova V, Geers M. Multi-scale continuous–discontinuous framework for computational-homogenization–localization. J Mech Phys Solids 2012;60(8):1486–507.
[40] Bahtiri B, Arash B, Scheffler S, Jux M, Rolfes R. A machine learning-based viscoelastic–viscoplastic model for epoxy nanocomposites with moisture content. Comput Methods Appl Mech Engrg 2023;415:116293.
[41] Li M, Wang B, Hu J, Li G, Ding P, Ji C. Artificial neural network-based homogenization model for predicting multiscale thermo-mechanical properties of woven composites. Int J Solids Struct 2024;301:112965.
[42] Yamanaka Y, Hirayama N, Terada K. Surrogate computational homogenization of viscoelastic composites. Internat J Numer Methods Engrg 2025;126(6):e70008.
[43] Al-Haik M, Hussaini M, Garmestani H. Prediction of nonlinear viscoelastic behavior of polymeric composites using an artificial neural network. Int J Plast 2006;22(7):1367–92.
[44] Haj-Ali R, Pecknold DA, Ghaboussi J, Voyiadjis GZ. Simulated micromechanical models using artificial neural networks. J Eng Mech 2001;127(7):730–8.
[45] Bishara D, Xie Y, Liu WK, Li S. A state-of-the-art review on machine learning-based multiscale modeling, simulation, homogenization and design of materials. Arch Comput Methods Eng 2023;30(1):191–222.
[46] Chen Y, Zhao Z, Li D, Guo Z, Dong L. Constitutive modeling for linear viscoelastic fiber-reinforced composites. Compos Struct 2021;263:113679.
[47] Daghia F, Lagache A, Di Gennaro L. Validation of a new viscoelastic model for unidirectional polymer matrix composites by analytical and numerical homogenisation. Eur J Mech A Solids 2023;100:104975.
[48] van der Sluis O, Schreurs P, Meijer H. Effective properties of a viscoplastic constitutive model obtained by homogenisation. Mech Mater 1999;31(11):743–59.
[49] van der Sluis O, Schreurs P, Brekelmans W, Meijer H. Overall behaviour of heterogeneous elastoviscoplastic materials: effect of microstructural modelling. Mech Mater 2000;32(8):449–62.
[50] Zhang L, Klimm WJ, Kwok K, Yu W. A nonlinear viscoelastic-viscoplastic constitutive model for epoxy polymers. In: AIAA sciTech 2022 forum. 2022, p. 1120.
[51] Liu Y, Van der Meer F, Sluys LJ, Fan J. A numerical homogenization scheme used for derivation of a homogenized viscoelastic-viscoplastic model for the transverse response of fiber-reinforced polymer composites. Compos Struct 2020;252:112690.
[52] Yue X, Guo R, An N, Zhou J. Modeling viscoelasticity–viscoplasticity of high-strain composites for space deployable structures. Int J Solids Struct 2025;308:113154.
[53] Lu P, Nan T, Liu H, Zhang Z, Yang Y, Chen Y, Zhang C. A viscoelastic–Viscoplastic constitutive model for fiber-reinforced composites with application to variable angle tow composites. Compos Commun 2025;102479.
[54] Chen Y, Nan T, Yun GJ, Zhang C. Micromechanical modeling of the viscoelastic–viscoplastic response of fiber-reinforced composites. Internat J Engrg Sci 2022;181:103767.
[55] Zhang X, Wang T, Yi Y, Mi X, Yang T, Chen W. Nonlinear viscoelastic-viscoplastic coupled behavior and mechanical model for substrates of flexible solar array. Internat J Numer Methods Engrg 2025;126(22):e70169.
[56] Gerritzen J, Gröger B, Zscheyge M, Hornig A, Gude M. 3D viscoelastic plastic model coupled with a continuum damage formulation for fiber reinforced polymers. Mater Des 2025;114969.
[57] Zhao F, Huang J, Yu S, Yu J, Guo L. A viscoelastic-plastic constitutive model for PEEK resin based on the physical model and artificial neural network. Int J Solids Struct 2025;113738.
[58] Block J, Straubel M, Wiedemann M. Ultralight deployable booms for solar sails and other large gossamer structures in space. Acta Astronaut 2011;68(7–8):984–92.
[59] Miled B, Doghri I, Delannay L. Coupled viscoelastic–viscoplastic modeling of homogeneous and isotropic polymers: Numerical algorithm and analytical solutions. Comput Methods Appl Mech Engrg 2011;200(47–48):3381–94.
[60] Hill R. The mathematical theory of plasticity. vol. 11, Oxford University Press; 1998.
[61] Hahn HT, Tsai SW. Nonlinear elastic behavior of unidirectional composite laminae. J Compos Mater 1973;7(1):102–18.
[62] Kawai M, Masuko Y. Creep behavior of unidirectional and angle-ply T800H/3631 laminates at high temperature and simulations using a phenomenological viscoplasticity model. Compos Sci Technol 2004;64(15):2373–84.
[63] Chen J, Sun C. A plastic potential function suitable for anisotropic fiber composites. J Compos Mater 1993;27(14):1379–90.
[64] Sun C, Chen J. A simple flow rule for characterizing nonlinear behavior of fiber composites. J Compos Mater 1989;23(10):1009–20.
[65] Yang J, Yang X, Zhu H, Shi D, Chen X, Qi H. The effect of off-axis angles on the mesoscale deformation response and failure behavior of an orthotropic textile carbon-epoxy composite. Compos Struct 2018;206:952–9.
[66] Dassault S. Abaqus 6.14 documentation. Simulia Systems, Providence, RI, USA; 2014.
[67] Yue X, Yue M, Ge Z, Yun D, Zhou J. A rational incorporation of hydrostatic stress into the rate theory models for fission-gas behavior in U3Si2 dispersion fuels. Mater Today Commun 2025;113600.
[68] Brown L, Long A. Modeling the geometry of textile reinforcements for composites: TexGen. In: Composite reinforcements for optimum performance. Elsevier; 2021, p. 237–65.
[69] Hamillage MY, Klimm W, Kwok K, Fernandez JM. Shape recovery simulation of viscoelastic thin-ply composite coilable booms. Acta Astronaut 2024;215:607–17.
[70] Fernandez JM, Murphey TW. A simple test method for large deformation bending of thin high strain composite flexures. In: 2018 AIAA spacecraft structures conference. 2018, p. 0942.